applied sciences

MDPI

Article

Thermographic Investigation on Fluid Oscillations and Transverse Interactions in a Fully Metallic Flat-Plate Pulsating Heat Pipe

Luca Pagliarini [1], Luca Cattani [1,*], Vincent Ayel [2], Maksym Slobodeniuk [2,3], Cyril Romestant [2] and Fabio Bozzoli [1,4]

[1] Department of Engineering and Architecture, University of Parma, 43121 Parma, Italy; luca.pagliarini@unipr.it (L.P.); fabio.bozzoli@unipr.it (F.B.)
[2] Pprime Institute, CNRS—ENSMA—Université de Poitiers, Av. Clément Ader 1, 86360 Chasseneuil-du-Poitou, France; vincent.ayel@ensma.fr (V.A.); maksym.slobodeniuk@ensma.fr (M.S.); cyril.romestant@ensma.fr (C.R.)
[3] IPSA, Direction de la Recherche et de l'Innovation de l'IPSA, 92120 Ivry-sur-Seine, France
[4] SITEIA.PARMA Interdepartmental Centre, University of Parma, 43121 Parma, Italy
* Correspondence: luca.cattani1@unipr.it

Abstract: The present investigation deals with the quantification of fluid oscillation frequencies in a metallic pulsating heat pipe tested at varying heat loads and orientations. The aim is to design a robust technique for the study of the inner fluid dynamics without adopting typical experimental solutions, such as direct fluid visualizations through transparent inserts. The studied device is made of copper, and it is partially filled with a water–ethanol mixture (20 wt.% of ethanol). Heat fluxes locally exchanged between the working fluid and the device walls are first assessed through the inverse heat conduction problem resolution approach by processing outer wall temperature distributions acquired by thermography. The estimated local heat transfer quantities are therefore processed to quantify the fluid oscillatory behavior in every device branch during the intermittent flow and full activation regimes, thus providing a deeper insight into the heat transfer modes. After dealing with a further validation of the inverse approach in terms of oscillation frequency restoration capability, the wall-to-fluid heat fluxes referred to each channel are processed by means of the wavelet method. Scalograms and power spectra of the considered signals are presented for a time-based analysis of the working fluid oscillations, as well as for the identification of dominant oscillation frequencies. Fluid motion is then quantified in terms of the continuity of fluid oscillations and activity of channels by applying a scalogram denoising technique named K-means clustering method. Moreover, a statistical reduction of the channel-wise dominant oscillation frequencies is performed to provide useful references for the interpretation of the overall oscillatory behavior. The link between oscillations and transverse interactions is finally investigated. The vertical bottom-heated mode exhibits stronger fluid oscillations with respect to the horizontal mode, with fluid oscillation frequencies ranging from 0.78 up to 1 Hz. Nonetheless, the fluid motion is more stable in terms of oscillation frequency between channels when the device operates in the horizontal orientation probably due to negligible buoyancy effects. Moreover, thermal interactions between adjacent channels are found to be stronger when the oscillatory behavior presents similar features from channel to channel in horizontal orientation. The proposed method for fluid oscillation analyses in fully metallic flat-plate pulsating heat pipes can be effectively adopted to other flat-plate layouts without any need for transparent windows, thus reducing the overall complexity of experimental set-ups and providing, at the same time, a good insight into the inner fluid dynamics.

Keywords: flat-plate pulsating heat pipe; infrared thermographic acquisitions; wavelet method; fluid oscillations; transverse conduction

check for updates

Citation: Pagliarini, L.; Cattani, L.; Ayel, V.; Slobodeniuk, M.; Romestant, C.; Bozzoli, F. Thermographic Investigation on Fluid Oscillations and Transverse Interactions in a Fully Metallic Flat-Plate Pulsating Heat Pipe. *Appl. Sci.* **2023**, *13*, 6351. https://doi.org/10.3390/app13106351

Academic Editor: Igor Pušnik

Received: 21 April 2023
Revised: 16 May 2023
Accepted: 18 May 2023
Published: 22 May 2023

Copyright: © 2023 by the authors. Licensee MDPI, Basel, Switzerland. This article is an open access article distributed under the terms and conditions of the Creative Commons Attribution (CC BY) license (https://creativecommons.org/licenses/by/4.0/).

1. Introduction

The self-sustained motion of the working fluid greatly affects the overall thermal behavior of passive two-phase heat transfer devices, such as heat pipes (HPs) and pulsating heat pipes (PHPs). In fact, in PHPs, fluid oscillations are responsible for efficient heat dissipation at the heated section (evaporator) [1]. Specifically, in such passive systems, the fluid flow is promoted by temperature differences between the evaporator and the cooled section (condenser) rather than external auxiliary equipment (such as pumps). Since the fluid is mainly saturated, thermal instabilities result in pressure differences which act as driving forces for its self-motion [2]. It is thus evident that such devices are governed by an extremely complex interplay between thermodynamic and fluid-dynamic behavior. The employment of HPs and PHPs has been found to be very attractive for many thermal management applications requiring a drastic reduction in electrical energy consumption [3]. Nevertheless, one of the main drawbacks of passive devices is represented by the need for a constant and self-induced backflow of liquid from the condenser to the evaporator, i.e., a continuously supplied evaporation process. While in HPs a persistent liquid flow to the evaporator is ensured by properly designed wick structures, such a phenomenon is only supported by non-equilibrium conditions in PHPs, thus largely increasing the complexity of their working behavior [4]. For this reason, the thermo-fluid dynamics underlying the oscillatory modes in PHPs are not yet completely understood despite the intensive experimental efforts of the last decades. In general, fluid oscillations are described in terms of amplitude, i.e., fluid displacement and frequency. However, a proper quantification of frequency in PHPs is hampered by the non-periodicity of fluid oscillations [5]. Consequently, all the oscillation frequencies experienced by the flow pattern during the PHPs operation are usually represented by a single frequency, named dominant (or characteristic) oscillation frequency, defined as a peak in the power spectrum of a given signal [6]. Generally, the dominant fluid oscillation frequency is evaluated by means of Fourier transform [7–10], short-time Fourier transform [11] or time-strip technique [12] on wall temperature measurements or optical acquisitions on the fluid flow. Perna et al. [6] suggested the use of the wavelet method for a reliable time-frequency localization of dominant fluid oscillation frequencies, which is not always obtainable from the Fourier or short-time Fourier transforms. In their analysis, the fluid pressure signals, measured at two different points of a multi-turn PHP channel and sampled at 200 Hz, were proven to be suitable for the fluid oscillations assessment. However, the intrusive insertion of pressure transducers inside the fluid stream is generally hard to achieve from a manufacturing standpoint. To deal with this issue, Pagliarini et al. [13] replicated the analysis presented in [6] on the same device under the same working conditions by adopting instead wall-to-fluid heat flux signals as inputs for the wavelet method, evaluated from thermographic acquisitions, i.e., non-intrusive measurements, on the outer wall surface. The outcomes denoted that the local wall-to-fluid thermal interactions allow for a similar evaluation of dominant fluid oscillation frequencies to that provided by pressure signals. In addition, the experimental approach reliably quantified the oscillatory behavior in every device branch, thus representing an effective solution for the study of PHPs when fluid pressure measurements in multiple branches cannot be achieved. Iwata et al. [14] performed a similar analysis to characterize the oscillatory behavior in a tubular micro-PHP tested in a vertical position. The IR acquisitions were performed within the condenser section of the device, dissipating heat to the environment by radiation and free convection with air. Fluid oscillations became stronger at high heat loads both in terms of power and frequency, and every channel exhibited similar oscillatory behavior.

While most of the fluid oscillation frequency investigations have dealt with tubular PHPs, i.e., PHPs constituted by a pipe arranged in a serpentine manner, some researchers have focused on the thermofluidic behavior of other configurations, such as flat-plate PHPs, i.e., PHPs with generally rectangular/squared channels that are directly machined on metallic/polymeric plates [15]. In particular, FPPHPs exhibit a rather different thermal response with respect to tubular layouts. First, the conduction through their solid domain promotes

heat dissipation at the evaporator, even though transverse interactions between adjacent channels may hamper the device's operation [16]. Secondly, the non-circular section of the channels may modify the overall thermofluidic behavior. Due to the manufacturing complexity of inserting pressure probes inside the fluid stream, the fluid-dynamic behavior of FPPHPs is commonly studied by means of direct fluid visualizations. Slobodeniuk et al. [17] investigated stopovers of a seven-turn FPPHP under micro-gravity conditions through high-speed visualization. By means of a liquid–vapor interfaces tracking technique, previously introduced by Pietrasanta et al. [18], the menisci displacement was assessed and both fluid velocity and fluid acceleration were evaluated. Miyazaki and Arikawa [19] highlighted that starting from the dried condition, the phase of liquid plugs oscillations is not independent in every channel, and the menisci displacement propagates in a waveform. Due to the spring effect of the vapor bubbles, the fluid motion is sequentially transmitted from one branch to another along the PHP. Moreover, they showed that the oscillation frequency is influenced by the heat flux and heat energy is accumulated in the solid walls. From a direct visualization of a horizontally oriented FPPHP, Borgmeyer and Ma [20] found that the nature of the working fluid significantly affects the oscillating motion of liquid slugs. With water, no oscillations were observed, whereas large oscillation amplitudes and velocities (up to 5 cm/s) were reached with ethanol under same operating conditions. On the other hand, Pagnoni et al. [21] found maximum velocities around 0.6 and 1 m/s, and frequencies from 2.5 up to 4 Hz, for heat powers of 80 W and 200 W, respectively, in their vertically oriented FPPHP with horizontal channels and filled with ethanol. From a comparison between a multi-turn, tubular PHP and a FPPHP having transparent inserts, Takawale et al. [9] observed that oscillation amplitudes increased with the heat load to the evaporator in both configurations, although the tubular PHP exhibited much larger amplitudes. The absolute measured fluid velocities were about 8 to 10 times higher than those inside the FPPHP. The tubular PHP denoted more vigorous, large-amplitude oscillations with respect to the flat-plate layout. Jun and Kim [22] proposed a mass-spring-damper model for the fluid displacement description in FPHPs during dry-out phases and until the large amplitude oscillations mode. The model was validated by coupling high-speed videos with fluid temperature/pressure measurements on a ten-turn micro FPPHP, thus highlighting optimal conditions for normal device operation in a horizontal orientation. Yoon and Kim [23] designed and experimentally validated, with rather good accuracy, a mass-spring-damper model that considered not only volume variations in slugs and plugs, but also mass variations due to evaporation/condensation phenomena. Such a model has also been proven to perform better than the usual ones where mass variations are generally neglected.

Although FPPHPs with transparent windows have been extensively studied in terms of flow characteristics, to the authors' knowledge, a significant amount of data regarding fluid oscillations in fully metallic devices is missing in the literature. This represents an extreme limitation for the deep understanding of FPPHPs heat transfer modes. On one hand, designing post-processing techniques for only direct visualizations precludes the possibility of extending the investigations to every possible device. On the other hand, the conductive phenomena largely occurring in FPPHPs might be influenced by the different thermal properties of transparent inserts, thus preventing robust comparisons with fully metallic devices. Moreover, such a lack of insight into fluid oscillation frequencies undermines the validation and improvement of existing numerical and theoretical models on FPPHPs. For instance, Dreiling et al. [24] designed a three-dimensional thermal conduction-based model for pseudo-steady state operation to predict the FPPHP thermal resistance. The effect of inner fluid oscillations has been considered negligible due to the high uniformity of wall temperature usually observed in flat layouts. However, such an assumption may not be always true, especially when the device undergoes strong transient behavior in terms of intermittent operation or the occurrence of local hot spots [25]. In [23], since the investigation was conducted for micro-geometries, the resulting fluid oscillation frequencies were found to be much higher than those observed in regular, metallic layouts, thus hampering the

capability of the adopted mass-spring-damper model to predict the oscillatory behavior in metallic FPPHPs. For the sake of completeness, it has to be stressed that some works have dealt with the direct observation of fluid motion inside fully metallic FPPHPs through neutron radiography [26–28]. However, such an experimental method is not easily implementable, especially due to the extremely high cost and complexity of instrumentations and peripheral facilities. Hence, the present work proposes a novel experimental approach for the evaluation of dominant fluid oscillation frequencies in fully metallic FPPHPs by means of infrared (IR) thermography. The aim is to provide a straightforward and effective technique for the estimation of fluid oscillation frequencies in fully opaque flat-plate layouts (i.e., where direct fluid visualizations cannot be carried out) to obtain interesting pieces of data regarding the inner fluid dynamics and to enlarge the overall literature dataset. The procedure is designed as an extension of the one presented in [13] for a metallic tubular PHP, as well as a natural evolution of the experimental work described in [29] on the same device under the same working conditions. Here, the authors thoroughly explained a novel method for the evaluation of wall-to-fluid heat fluxes along the adiabatic section of an eight-turn FPPHP made of copper, starting from IR acquisitions on the outer wall surface at varying heat loads to the evaporator and tilt angles. In the current analysis, the evaluated wall-to-fluid heat flux distributions are used as inputs for the wavelet method to quantify dominant fluid oscillation frequencies in every branch of the device. The time evolution of oscillatory behavior is further quantified by such a non-intrusive technique, which does not rely on transparent windows nor on fluid pressure/temperature sensors. A statistical reduction of the results provides a complete description of the overall FPPHP oscillatory behavior, in accordance with the global and local heat transfer characteristics highlighted in [29]. Finally, a link between transverse interactions and fluid oscillations is presented to provide an overview on the thermo-fluid dynamics of the studied device. To the authors' knowledge, this represents one of the first attempts of experimentally quantifying fluid oscillatory features in metallic FPPHPs through infrared observations. The newly proposed method, based on the reduction in local heat fluxes for the estimation of fluid oscillation frequencies in FPPHPs, provides a good degree of insight into the oscillatory behavior of the investigated devices without any direct fluid visualization. This strongly simplifies the experimental set-ups generally used for the study of fluid dynamic quantities in such devices. The adopted technique can be applied to a wide range of other flat-plate systems having fully metallic walls for a robust and repeatable study of the inner fluid dynamics, i.e., even when no transparent windows are present.

2. Experimental Apparatus

The studied device is an eight-turn FPPHP (overall dimensions: 80 × 200 × 4 mm) entirely made of copper and with 3 × 3 mm^2 squared channels (Figure 1a). One side of the device is coated with a black high-emissivity paint (ε = 0.92) to allow thermographic measurements on the outer wall temperature within the adiabatic section. This first plate was covered and brazed with tin to a second copper plate having the same dimensions and 0.5 mm of thickness. The reader is referred to [30] for the description of the manufacturing process.

The opaque paint emissivity was evaluated by performing dedicated IR acquisitions on a coated isothermal surface (same opaque paint, at controlled temperature and monitored through thermocouples). The emissivity parameter set in the IR camera software was regulated until a match between the temperature measured by thermocouples and the one by the infrared camera was reached in the range of absolute uncertainty of the camera (±1 °C). Since the emissive layer had a thickness lower than 100 μm, its thermal resistance was considered negligible, thus reasonably assuming that the temperature measured on top of the coating corresponded to the one of the device's surfaces. To guarantee full accessibility of the adiabatic section in terms of thermographic measurements, such a portion was not covered with insulating material.

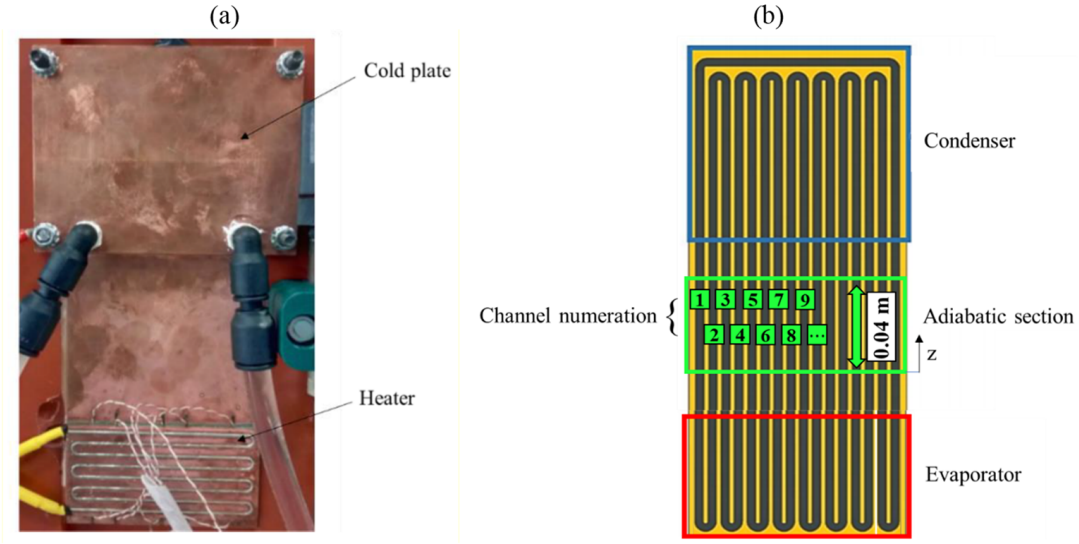


Figure 1. Rear side of the studied FPPHP (**a**); sketch of the machined path for the working fluid and reference for the evaporator/condenser/adiabatic sections' locations, as well as for the channels' numeration and area framed by the MWIR camera (green box) (**b**).

Power is provided to the evaporator zone by a wire electrical heater (Thermocoax® Type NcAc15, 1 mm external diameter), connected to an electrical power supply (ELC® ALR3220, ±10 mV). The condenser section is cooled by a loop connected to a copper cold plate (width: 100 mm, length: 80 mm), directly brazed on the rear side of the FPPHP (Figure 1a). The loop temperature is controlled by a cryostat (Huber® CC240 wl). Two pipes are brazed on the top and bottom sides of the device, allowing the filling and vacuuming of the system, respectively. The FPPHP was filled with a water/ethanol mixture (20 wt.% of ethanol) with a filling ratio of 50% (at ambient temperature). Specifically, such a working fluid was chosen since it led, as proven in [30]—for the same FPPHP and among a selection of various fluids (pure water, pure ethanol, water aqueous mixtures with 5% of butan-1-ol, 5% of butan-2-ol, 16% and 20% of ethanol, 28% of methanol and 0.5% of surfactants—Tween® 20 and Tween® 40)—to better thermal performances of the device at different tilt angles and working conditions, making the adopted water/ethanol aqueous mixture suitable for robust and repeatable fluid oscillation analyses.

Part of the adiabatic section was monitored by means of a high-speed Medium Weave InfraRed camera (MWIR, FLIR® SC5500, 320 × 256 pixels resolution). In Table 1, the uncertainties of the adopted experimental equipment are listed.

Table 1. Experimental equipment and corresponding uncertainty and operation range.

Experimental Equipment	Uncertainty	Operating Range
Power supply	±2 W	50–250 W
Cryostat	±1 °C	20 °C
MWIR camera	Absolute: ±1 °C Sensitivity: <25 mK	3–5 µm 5 °C–300 °C

The reference for the channels' numeration is reported in Figure 1b, together with the heat transfer sections, i.e., evaporator (red box, 40 mm long) and condenser (blue box, 80 mm long), and the area framed by the camera (green box, 40 mm long). The reference for the axial direction z is also shown. The analysis was performed for two device orientations, namely the vertical bottom heated mode (BHM) and the horizontal orientation (Figure 2), and different heat loads Q applied to the evaporator, spanning from 50 to 250 W. During the tests, IR acquisitions, each lasting 20 s, were performed with a sampling frequency of 50 Hz in the so-called pseudo-steady state operation of the device,

i.e., after about 30 min from the delivery of each power step. Specifically, IR thermography was chosen, among other experimental methods, since it provided an accurate estimation of wall temperature variations for effective wall-to-fluid heat flux evaluations. In fact, using other experimental means, such as thermocouples attached on the outer wall of the device, would lead to a poorer assessment of thermal transients due to intrinsic limitations, including slower thermal response, lower accuracy and high contact resistance. When carrying out IR acquisitions, the effects of IR radiations coming from the environment and partially reflected by the surface of interest (belonging to the coated adiabatic section of the device) were considered as negligible, i.e., they did not substantially affect the IR measurements. This reasonable assumption is supported by the fact that during the tests, the device wall temperature was at least 13 °C higher than the environmental one, and the adopted, opaque coating was poorly reflective.

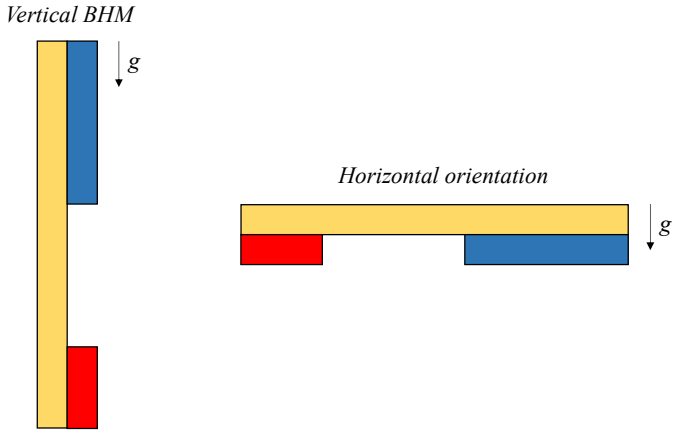


Figure 2. Investigated device orientations with respect to the gravity field.

3. Methods

3.1. Wall-to-Fluid Heat Flux Estimation

The procedure for the estimation of the heat flux exchanged between the FPPHP thin walls and the working fluid is based on the post-processing of the thermographic data by the inverse heat conduction problem (IHCP) resolution approach, coupled with a three-dimensional Gaussian filter for the regularization of the raw space-time temperature maps. Such a procedure is carried out within the adiabatic section of the device, and it is thoroughly explained in [29], together with its error estimation. In Figure 3, the areas of interest for the wall-to-fluid heat flux estimation, i.e., where the FPPHP channels present thin walls, are highlighted in red.

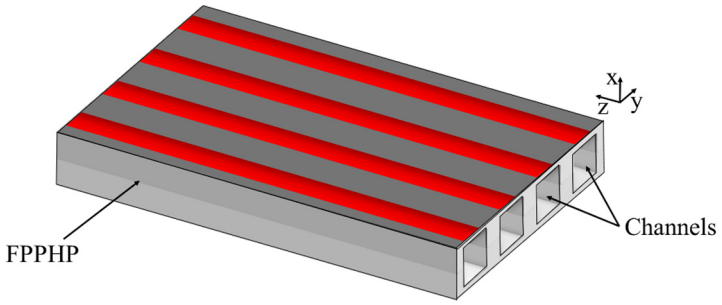


Figure 3. Three-dimensional sketch of a FPPHP portion within the adiabatic section; in red, areas of interest for the wall-to-fluid heat flux evaluation.

The resulting wall-to-fluid heat flux distributions q are bi-dimensional maps referred to each FPPHP channel over 0.04 m (length of the section of interest) and 20 s (duration of each MWIR acquisition). In particular, by considering the energy balance equation in transient

conditions at the thin wall element and by rearranging all the terms, the wall-to-fluid heat flux finally assumes the following formulation [29]:

$$q = s\left(\rho c_p \frac{\partial T}{\partial t} - k\frac{\partial^2 T}{\partial y^2} - k\frac{\partial^2 T}{\partial z^2}\right) + h_{env}(T - T_{env}) \quad (1)$$

where s is the wall thickness, ρ, c_p and k are density, specific heat and conductivity of copper, respectively, h_{env} is the outer heat transfer coefficient by free convection and radiation to the environment, and T_{env} is the environmental temperature. To obtain consistent values of heat flux q, the input temperature is filtered by following the steps below [29]:

- The three-dimensional, raw space-time temperature map is converted to the frequency domain by the discrete fast Fourier transform (DFFT);
- The transfer function for the Gaussian filter is applied to the frequency image of the input temperature map. A first attempt cut-off frequency is initially guessed;
- The temperature map is converted back to the space-time domain by applying the inverse DFFT;
- The residual between the raw input temperature map and the filtered temperature is computed;
- Steps 2–4 are iteratively replicated by varying the cut-off frequency until the evaluated residual equals the standard deviation of the raw temperature data, σ = 0.04 K (i.e., fulfilment of the Morozov's discrepancy principle [31]).

The goodness of the estimation procedure is therefore assessed by means of the following steps [29]:

- The direct problem is implemented in a COMSOL Multiphysics® environment. The solid domain of the device within the adiabatic section is simulated by using, as a boundary condition at the inner wall–fluid interface, a given space-time heat flux distribution that reflects the one exchanged in the real device. Equations for three-dimensional transient conduction are solved by the in-built solver;
- The synthetic temperature distribution resulting from the simulation is then spoiled with a noise level equal to the standard deviation of the raw data, and processed by means of the filtering technique;
- The wall-to-fluid heat flux is estimated back by means of Equation (1), i.e., leading to the inverse problem solution. The estimated wall-to-fluid heat flux is therefore compared with the one given as a boundary condition in Step 1, allowing the evaluation of the estimation error for the procedure (quantified in [29], equal to about 15% of the heat flux given in Step 1).

3.2. Oscillation Frequency Estimation

The fluid oscillation frequencies were evaluated starting from the wall-to-fluid heat flux distributions (Section 3.1), since the local thermofluidic interactions were believed to be strictly linked to the heat dissipation process underlying the FPPHP operation [13,32]. As already stated, the oscillatory behavior quantification was based on the wavelet method; in particular, according to Perna et al. [6], the Morlet wavelet, the shape of which is defined by Equation (2) for dimensionless time η and the characteristic parameter ω_0, was adopted.

$$\psi(\eta) = \frac{1}{\sqrt{\pi}} e^{-\frac{\eta^2}{2}} e^{i\omega_0 \eta} \quad (2)$$

The wavelet transform of a time-dependent signal $g(t)$ reads as [33]

$$W_\psi(a,\tau) = \frac{1}{\sqrt{a}} \int_{-\infty}^{\infty} g(t)\psi^*\left(\frac{t-\tau}{a}\right) dt \quad (3)$$

where a and τ are the wavelet scale (dilation of the wavelet function) and time shift, respectively, and the superscript * denotes the complex conjugate. The term $1/\sqrt{a}$ is due

to the adopted L1 normalization of the wavelet, used for comparison purposes between different scales. The output of the wavelet analysis is the so-called magnitude scalogram, defined as the absolute value of the wavelet transform, plotted as a function of frequency and time. In particular, it represents the power related to each frequency over the sample duration. Such a power is strictly linked to the oscillation amplitude of the signal; in fact, high-amplitude oscillations result in high powers in the scalogram. On the other hand, the power spectrum referred to as the considered signal is defined as the time integral of the magnitude scalogram, for every frequency. While the scalogram describes the time evolution of the characteristic frequencies underlying the considered oscillatory phenomenon, the power spectrum allows for the identification of the dominant frequency related to the considered sample (identified by a peak in the power spectrum).

The wavelet parameters adopted in the present analysis are listed in Table 2. In particular, these parameters were chosen to guarantee a good trade-off between the frequency and time resolution of the method.

Table 2. Parameters used for the wavelet method.

A [1/Hz]	71
ω_0 [rad/s]	2π
f_{min} [Hz]	0.1
f_{max} [Hz]	18

4. Validation of the Dominant Frequency Estimation Procedure

The method of Section 3.2 was validated following a similar validation procedure to that presented in [29] and summarized in Section 3.1. Direct simulations were implemented in a COMSOL Multiphysics® environment to solve conduction heat transfer equations within the FPPHP solid domain. In particular, the same analytical heat flux distributions q_{exact} used for the validation procedure of [29] were given as a boundary condition at the wall–fluid interfaces. Specifically, the guessed distribution for the analytical heat flux q_{exact} assumed the following sinusoidal form [29]:

$$q_{exact} = Amp \cdot \cos(2\pi t \cdot f - \varphi) + \frac{Amp}{2} - \frac{z}{H} \cdot Amp \quad (4)$$

where Amp is the heat flux amplitude in W/m^2, f is the oscillation frequency in Hz, φ is the phase shift (different from channel to channel to reflect the oscillatory behavior in the real device), z is the axial coordinate and H is the length of the portion of interest within the adiabatic section. The reader is referred to [29] for deeper details on the procedure.

The resulting synthetic temperature maps were therefore spoiled with noise, filtered and used as inputs for the inverse procedure to evaluate back the heat flux, $q_{restored}$. In other words, noisy temperature distributions were used as inputs for Equation (1), solved through the finite element method. However, while in [29] the validation procedure was focused on the percentage error estimation in terms of amplitude of the restored heat fluxes with respect to the exact ones (i.e., the guessed ones), the present validation aims at considering differences in oscillation frequency between q_{exact} and $q_{restored}$. Hence, q_{exact} and $q_{restored}$ were used as inputs for the wavelet method.

In Figure 4, q_{exact} (amplitude Amp = 2000 W/m^2, frequency f = 1.2 Hz) is shown, together with the wavelet method outputs. Due to the fact that the analytical formulation of q_{exact}, for which the time-dependent signal is presented in Figure 4a, is a sinusoid having a fixed frequency over time (please refer to [29]), the scalogram (Figure 4b) exhibits the same signal power (described by the color bar on the right) at each time instant of the observation window. It has to be stressed that the white dashed lines in scalograms delimit what is known as cone of influence (COI) [34]. Specifically, the COI highlights areas (grey-shaded) potentially affected by edge-effects, i.e., where the wavelet extends over the boundaries of the considered time interval, and they might not be representative of an accurate time-frequency description of the considered samples. For this reason, the power

spectrum evaluation does not consider such areas when integrating the power related to each frequency over time. In Figure 4c, the power spectrum is reported: here, the power related to low (<0.8 Hz) and high (>2 Hz) frequencies P_w is null, while it increases as long as the natural frequency of the treated signal (1.2 Hz) is approached. The absolute maximum of the power spectrum is found at 1.23 Hz. Hence, the error for the dominant frequency estimation procedure, i.e., the frequency resolution of the wavelet method for the present analysis, was assessed to be equal to 0.03 Hz. Such an error is intrinsic in the wavelet approach due to the shape of the considered wavelet function, having coefficients listed in Table 2. The lower limit of 0.5 Hz for the frequency scales has been chosen due to the limited observation window (20 s), which prevents the detection of a sufficient number of oscillations at lower frequencies, undermining the reliability of the method.

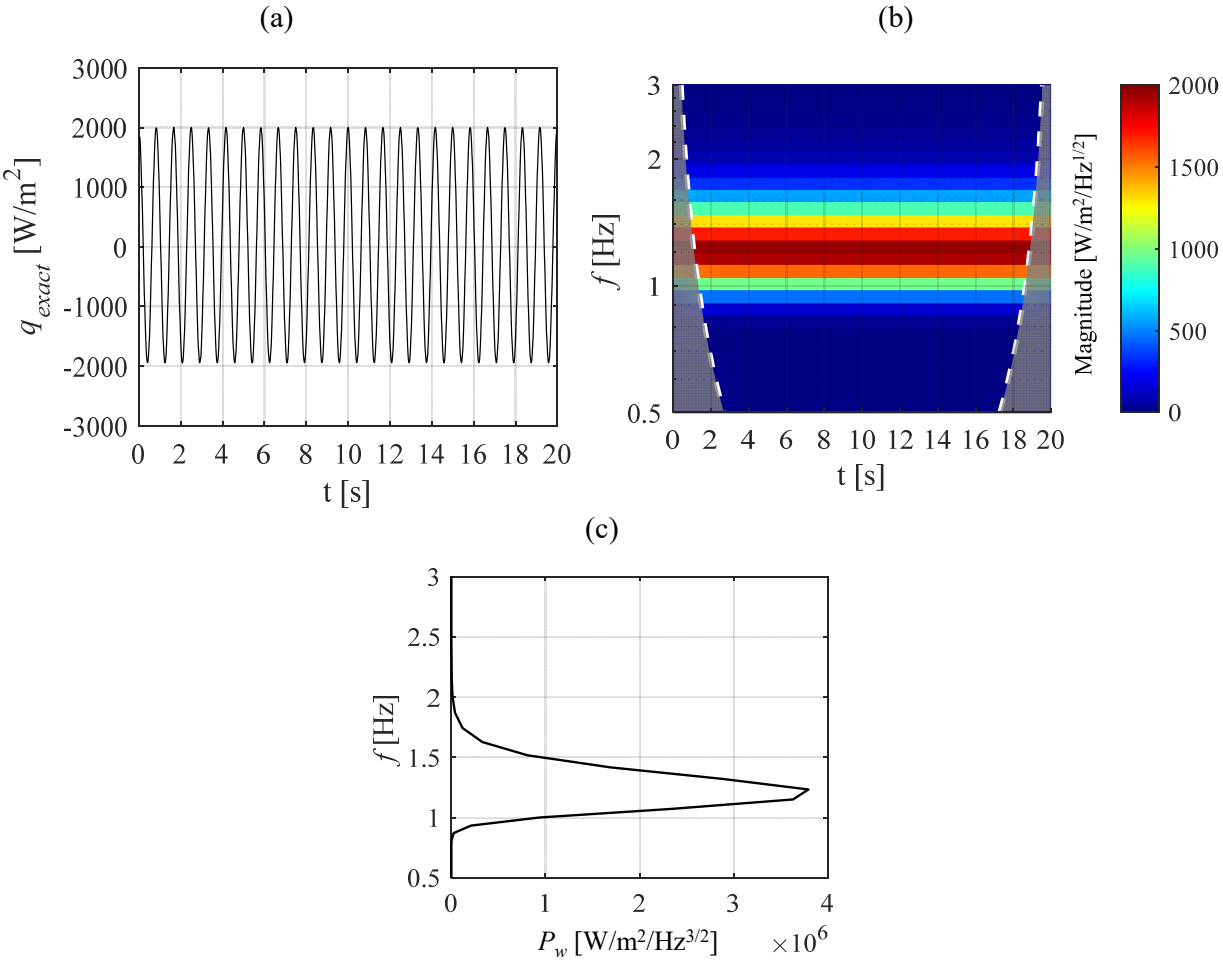


Figure 4. Exact heat flux over time (Amp = 2000 W/m^2, f = 1.2 Hz), used as input for the wavelet method (**a**); corresponding scalogram (**b**) and power spectrum (**c**).

In Figure 5, the same frequency analysis is presented for the restored heat flux referred to noise level σ = 0.04 K (noise level of the experimental set-up, as defined in [29]). The scalogram of Figure 5b, when compared to that of Figure 4b, suggests that some low- and high-frequency components are introduced by the restoration procedure. In fact, the scalogram is no longer represented by just a clear, high-power horizontal band, but some other low/average-power spots are perceivable. This effect is clearly noticeable in the power spectrum (Figure 5c), where its maximum decreases of about 20% of the Pw peak in Figure 4c mean that the power of the exact signal has been scattered over a wider range of frequencies. However, the maximum of the power spectrum is still at 1.23 Hz, suggesting that no significant errors are introduced by the heat flux restoration in terms of dominant frequency estimation. Such a remark was verified for all the considered q_{exact} and

$q_{restored}$, thus further proving that the presented procedure outcomes are not substantially dependent on the amplitude nor on the natural frequency of q_{exact}.

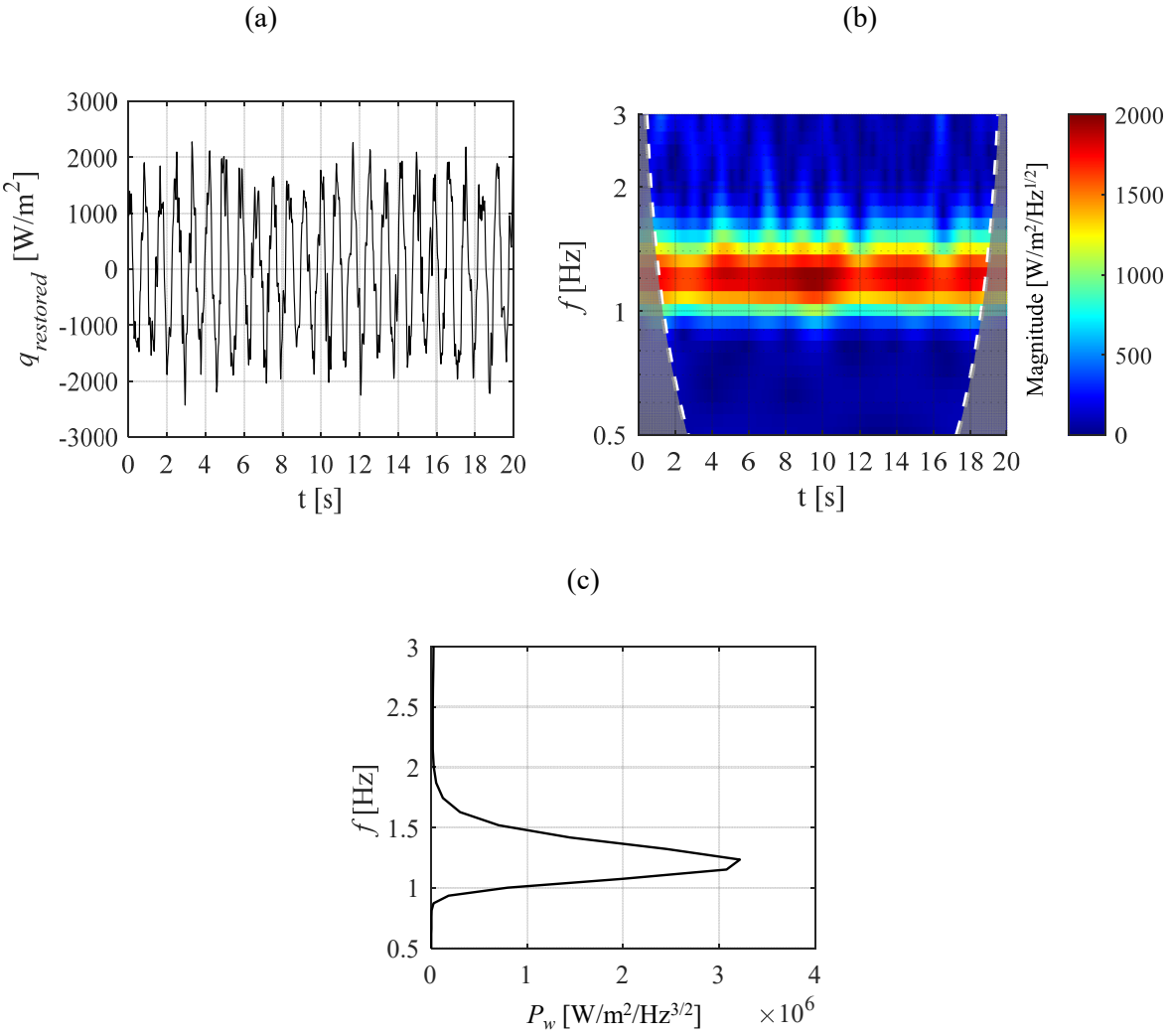


Figure 5. Restored heat flux, used as input for the wavelet method (**a**); corresponding scalogram (**b**) and power spectrum (**c**).

5. Results and Discussion

5.1. Fluid Oscillatory Behavior

The local thermal interactions between the working fluid and the FPPHP wall are representative of the fluid motion, i.e., fluid oscillations, inside the device, as demonstrated in [13]. Hence, the wavelet approach was used for the evaluation of dominant frequencies f_d in the overall studied device, i.e., every FPPHP channel, by adopting wall-to-fluid heat flux distributions for single axial coordinates over time. In Figure 6, the post-processed heat flux signal referred to z = 0.02 m for channel 8 (reference of Figure 1b) and Q = 100 W in the horizontal orientation is shown as a sample for the wavelet method outcomes understanding of experimental data.

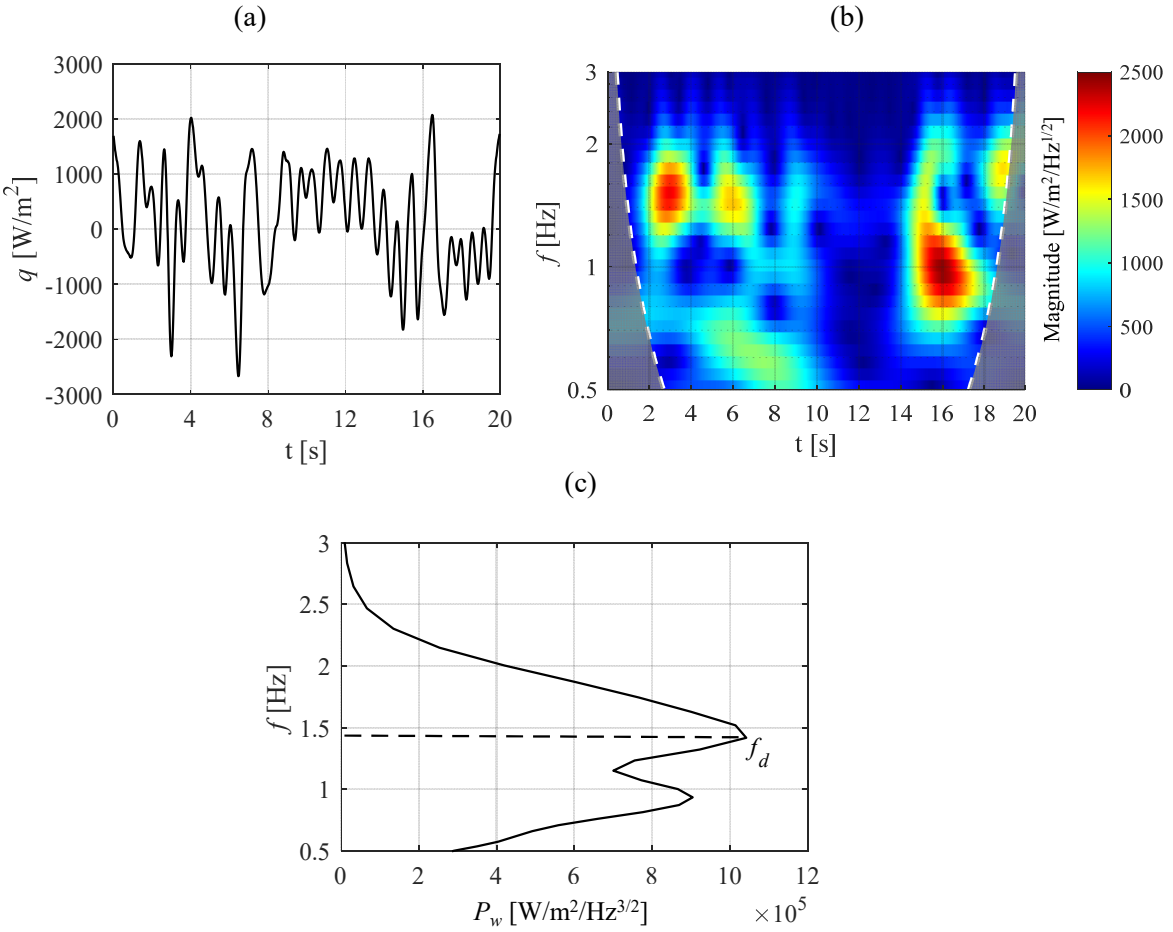


Figure 6. Heat flux for a single axial coordinate referred to channel 8 (z = 0.02 m), Q = 100 W, horizontal orientation (**a**), corresponding scalogram (**b**) and power spectrum (**c**).

The experimental-based signal (Figure 6a) highlights non-fixed amplitude and oscillation frequency over time. In fact, the scalogram of Figure 6b exhibits scattered spots having different power in the range from 0.8 to 2 Hz. From 0 to about 10 s, the high-power spots are mainly present around 1.5 Hz, denoting that the heat flux, i.e., the working fluid, oscillates with great amplitude at that frequency. From 10 to 14 s, the scalogram does not present significant power spots, thus suggesting the occurrence of weak heat flux oscillations. From 14 to 18 s, a high-power spot is perceivable around 1 Hz, denoting a substantial change in terms of oscillation frequency of the heat flux. Such a time change in oscillation frequency is also clear in the power spectrum (Figure 6c), where two peaks are present: one at about 1 Hz and one at about 1.5 Hz. Here, although there is a short-time change in oscillatory behavior, the heat flux mainly oscillates with variable amplitudes at about 1.5 Hz over the entire observation window, and the absolute maximum of the power spectrum is located around such frequency. In particular, the dominant oscillation frequency f_d of the signal is found at about 1.45 Hz.

It has to be pointed out that since the heat flux distributions evaluated in the present device significantly vary with space [29], the wavelet method may provide different results depending on the considered axial coordinate. To investigate such dependency, the wall-to-fluid heat flux signals related to a single channel at different z coordinates were used as inputs for the wavelet approach, and the resulting power spectra were therefore compared. In Figure 7, such a comparison was carried out for channel 9 at z = 0.01 m, z = 0.02 m and z = 0.03 m, and both device orientations at Q = 250 W. Here, despite different amplitudes of the wall-to-fluid heat fluxes of Figure 7a–c, their oscillatory trends over time do not present any dissimilarities from axial point to axial point. In fact, all the power spectra

of Figure 7b–d exhibit absolute peaks in correspondence with the same frequency, thus highlighting same the dominant frequency regardless of the considered axial position. For this reason, every processed heat flux was chosen, for the present analysis, to be at z = 0.02 m for every channel, representative of all other z coordinates.

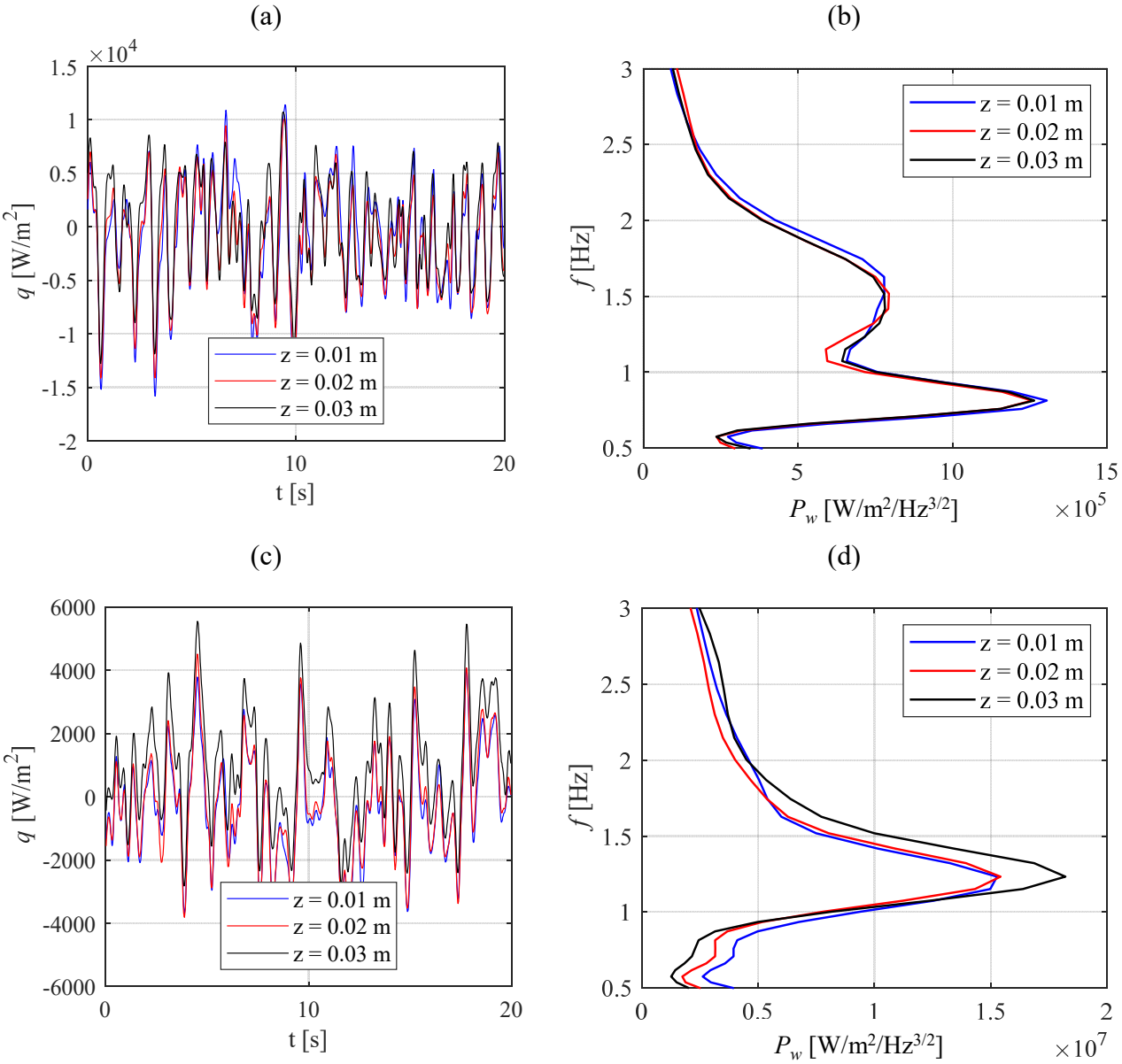


Figure 7. Wall-to-fluid heat flux signals over time related to channel 9 and Q = 250 W for three different axial coordinates and corresponding power spectra; vertical BHM (**a**,**b**) and horizontal orientation (**c**,**d**).

5.2. Channel-Wise Frequency Analysis

The wavelet method was extended to the heat flux signals referred to all the FPPHP branches, thus assessing channel-wise fluid oscillation frequencies at varying heat loads and orientations.

In Figure 8, the scalograms referred to three meaningful channels, namely channels 4, 8 and 12 (Ch4, Ch8 and Ch12, respectively), which are shown for the vertical BHM at power inputs equal to 50 W, 150 W and 250 W. Specifically, the three channels only were chosen to achieve a good trade-off between a clear spatial overview of the global oscillatory behavior in the studied device and a better readability of the discussion. The

power spectra related to every FPPHP channel are further presented for a comprehensive description of the oscillatory behavior in Figure 9 for the three considered heat loads. Note that magnitude scalograms in Figure 8 and power spectra in Figure 9 present, respectively, the same scale for better comparison. In Figure 8, Q = 50 W, the scalogram of Ch4 exhibits a medium-power area during the first seconds of acquisitions, suggesting the presence of weak oscillations. On the contrary, Ch8 and Ch12 do not present any significant power spots except for some low-power areas, thus highlighting a near absence of fluid motion. Such evidence is confirmed by the power spectra of Figure 9 (Q = 50 W), which are flat for most of the channels, i.e., no fluid oscillations can be perceived in almost the whole device. As the power input to the evaporator increases to 150 W, the scalograms of Figure 8, referred to the vertical BHM, present more persistent medium-power areas over time; additionally, all the power spectra of Figure 9 (Q = 150 W) exhibit perceivable peaks, suggesting that the fluid oscillates in every branch with dominant frequencies mainly below 1 Hz. For the maximum provided power input (Q = 250 W), the scalograms of Figure 8 highlight many high-power spots, denoting strong fluid oscillations over time. Nevertheless, the power spots are referred to different frequencies, suggesting that the oscillatory behavior is not stable over the observation window. The presence of strong oscillations described by high-power spots is confirmed by the power spectra of Figure 9 (Q = 250 W), which assume high peaks of P_w. Their absolute maxima are furthermore scattered within a wide range of frequencies between 0.6 and 1.6 Hz, thus denoting greatly different dominant fluid oscillation frequencies from channel to channel. The observed progressive increase in fluid motion in every channel confirms the typical flow regimes in PHPs [35–37]: at low heat loads, the device operation is mainly intermittent, presenting fluid oscillations in few channels; meanwhile, at high heat loads, every branch presents strong oscillations, although they are not persistent over the observation window.

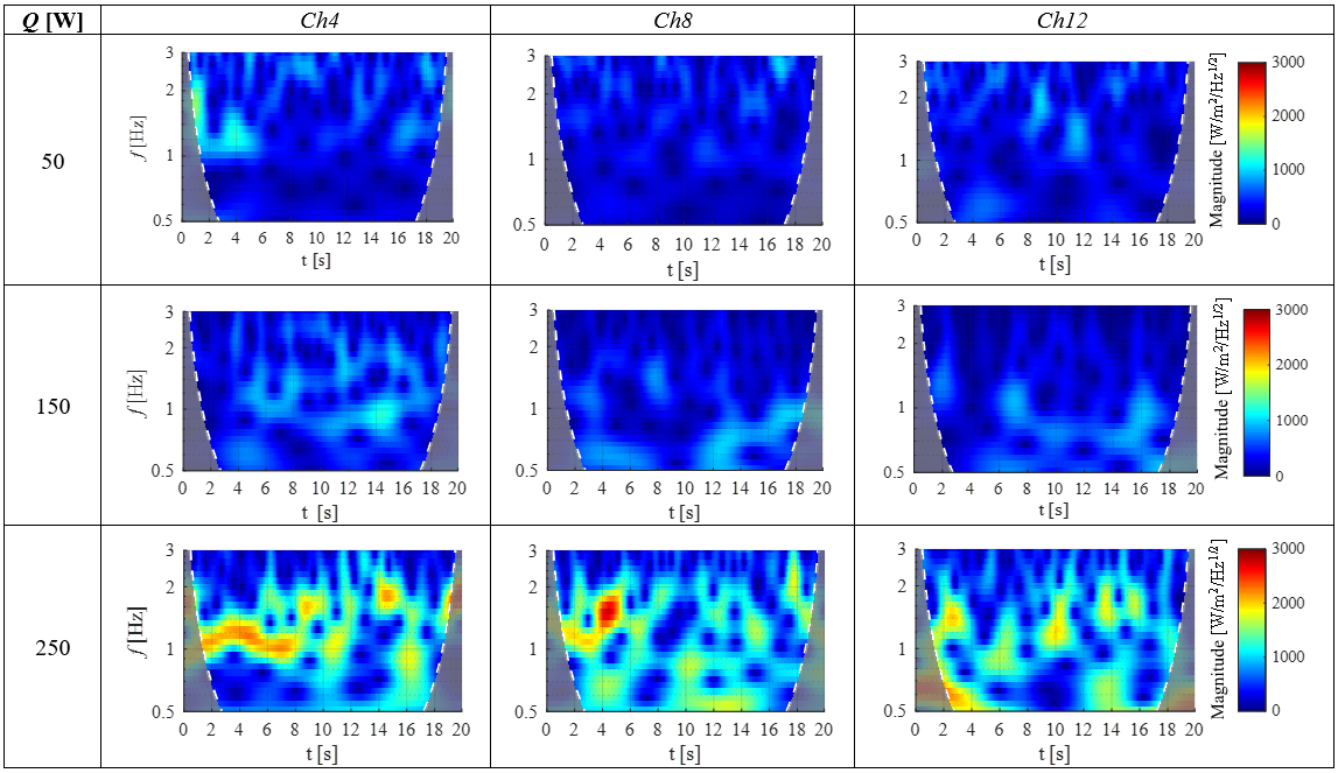


Figure 8. Wavelet scalograms for channels 4 (Ch4), 8 (Ch8) and 12 (Ch12) of the wall-to-fluid heat fluxes for the fixed axial coordinate z = 0.02 m at different heat loads to the evaporator (vertical BHM).

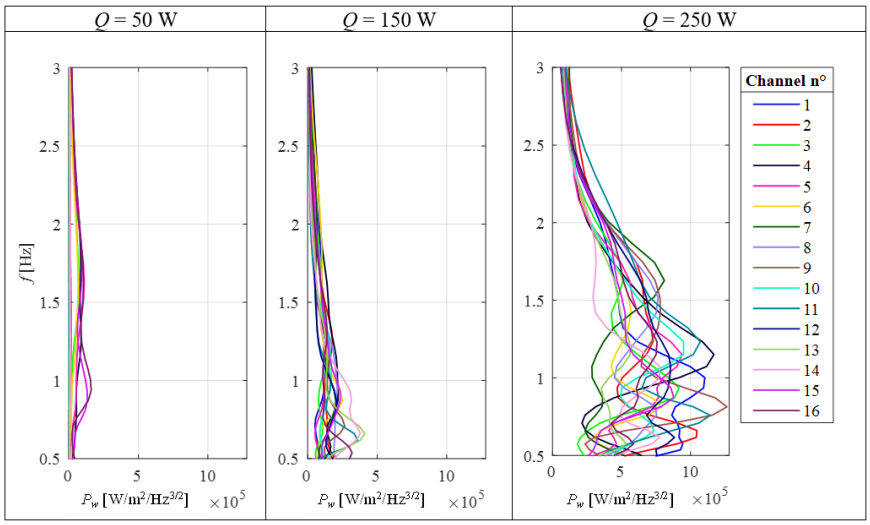


Figure 9. Power spectra of the wall-to-fluid heat fluxes for the fixed axial coordinate z = 0.02 m related to every FPPHP channel at different heat loads to the evaporator (vertical BHM).

Again, the scalograms and power spectra scale are adjusted to match the one at the highest heat load to the evaporator (Q = 250 W) to allow for a better and more straightforward comparison between different power inputs.

In Figure 10 at Q = 50 W, the scalograms do not present any significant power spots, denoting either the absence of fluid motion or very weak and intermittent oscillations. The device inactivity over the observation window is additionally highlighted by a complete absence of peaks in the power spectra of Figure 11 (Q = 50 W). It has to be stressed that since the color and Pw scales of the provided scalograms and power spectra are adjusted for comparison to match the ones at the highest power input, the values seem to be generally null. However, by observing, in Figure 12, a representative scalogram of Ch 4, Figure 10, 50 W, having an adjusted color scale around zero, it can be noted that the graph presents non-null power areas. Nonetheless, such non-null, low-amplitude regions account for residual noise in the input heat flux data rather than actual fluid oscillations. The same conclusion can be drawn for the other scalograms at 50 W, horizontal orientation, thus confirming the absence of fluid motion in the considered channels for the analyzed heat load. Such a remark agrees with what was observed in the previous literature [30,38,39], where operating FPPHPs in a horizontal orientation led to delayed start-ups at higher power inputs due to a lack of pumping forces assisted by gravity effects.

For Q = 150 W, the scalograms of Figure 10 exhibit medium-power stripes which persist with continuity during almost the whole acquisition in the considered channels, except for some higher-frequency spots that are especially evident for Ch4. High P_w are clearly noticeable from the power spectra of Figure 11 (Q = 150 W), confirming the presence of regular fluid oscillations with dominant frequencies around 0.9 Hz. At 250 W, the scalograms of Figure 10 show high-power spots which replicate at almost the same frequency over time, denoting the time regularity of the strong fluid oscillations occurring in such operating conditions. Such vigorous fluid oscillations in every FPPHP channel are also clear from the power spectra high peaks of Figure 11 (Q = 250 W), with dominant frequencies around 1.2 Hz. It is worth noting that, contrarily to the vertical BHM orientation, the peaks of P_w span a much narrower range of frequencies for every channel in the horizontal orientation for medium/high power inputs. This might be due to the fact that the buoyancy forces acting on the fluid in BHM increase the complexity of the device's operation and, consequently, of its oscillatory behavior. In fact, in the vertical BHM, a transition between slug-plug and semi-annular flow may occur, especially due to the squared section of the present FPPHP channels [16,40,41], thus increasing the chaoticity of the thermofluidic wall-to-fluid interactions. On the contrary, in the horizontal orientation, the flow pattern could probably be only slug-plug even for high power inputs to the

evaporator, i.e., high inertial forces on the fluid driven by damped oscillations of the vapor bubbles, thus resulting in a similar oscillatory behavior between every FPPHP branch. In fact, a slug-plug flow is more likely to occur in a horizontal orientation due to absence of buoyancy forces which tend to deform the liquid–vapor interfaces. For instance, Ayel et al. [42] observed a slug-plug flow during microgravity experiments on a closed-loop FPPHP with channel dimensions of 2.5 × 2.5 m^2 and FC-72 as a working fluid. Of note, weightlessness acts similarly to the horizontal orientation in terms of the negligible effects of buoyancy forces on the fluid stream, as proven in [43]. In [42], when a transition from hyper-gravity to microgravity occurred, the flow pattern varied from annular to slug-plug, confirming the higher stability of fluid menisci and overall fluid flow observed during horizontal operation in the present investigation.

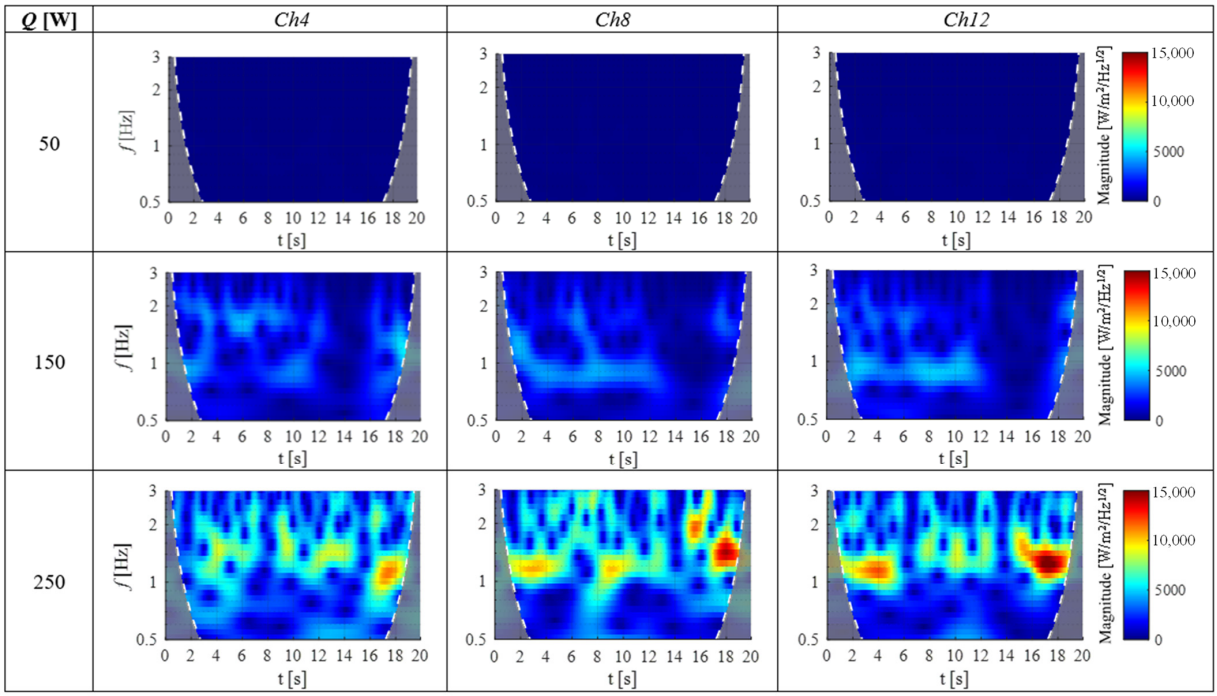


Figure 10. Wavelet scalograms for channels 4 (Ch4), 8 (Ch8) and 12 (Ch12) of the wall-to-fluid heat fluxes for the fixed axial coordinate z = 0.02 m at different heat loads to the evaporator (horizontal orientation).

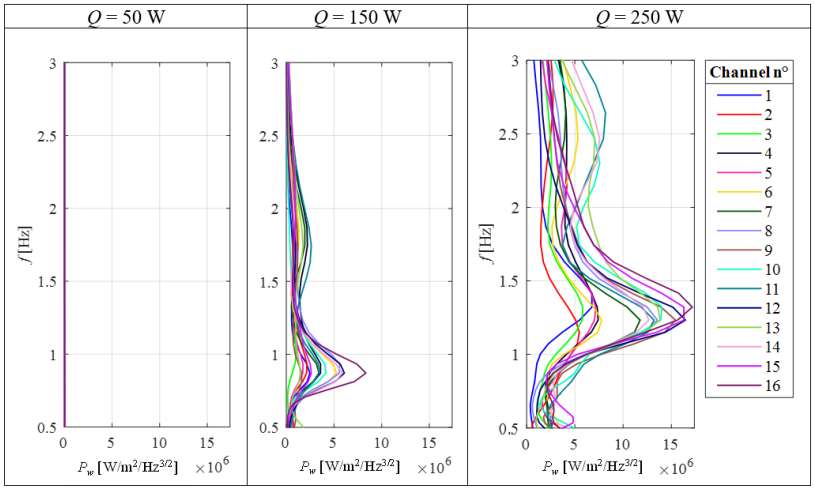


Figure 11. Power spectra of the wall-to-fluid heat fluxes for the fixed axial coordinate z = 0.02 m related to every FPPHP channel at different heat loads to the evaporator (horizontal orientation).

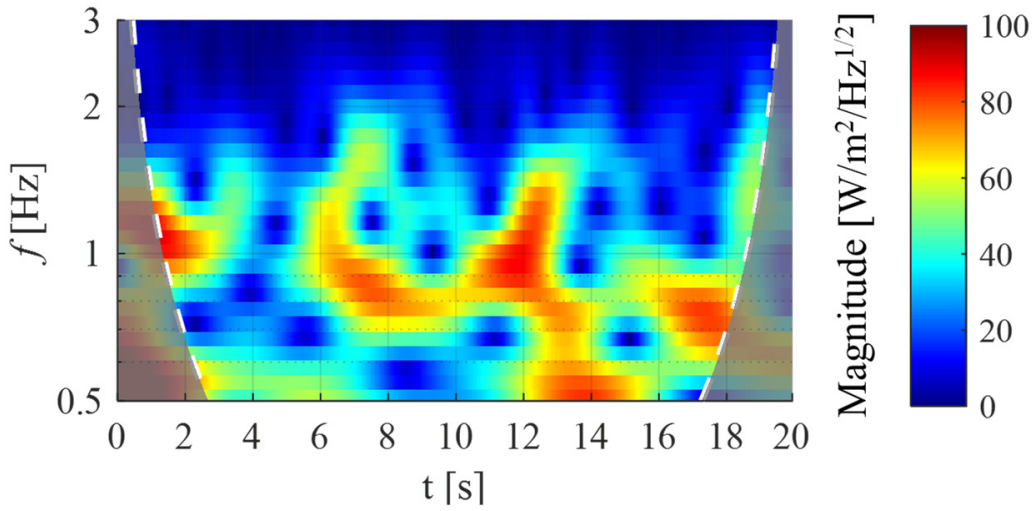


Figure 12. Scalogram of Figure 10, *Ch 4*, having adjusted color scale around the zero value; low-power areas are present due to residual noise in the input heat flux rather than actual oscillations of the working fluid.

To clearly provide a quantitative description of the channel-wise oscillatory behavior, all the evaluated dominant oscillation frequencies from the power spectra curves of Figures 9–11 are listed in Tables 3 and 4 for the vertical BHM and horizontal orientations, respectively.

Table 3. Dominant oscillation frequencies evaluated in the vertical BHM orientation for every channel at varying heat load. Dashes stand for absence of dominant fluid oscillation.

f_d [Hz]	Q [W]						
Channel	***50***	***70***	***90***	***120***	***150***	***200***	***250***
1	-	-	0.81	1.15	1.07	1.32	1
2	1.15	-	0.81	0.58	1.23	1.07	0.66
3	1.63	0.66	0.66	0.71	1.23	0.71	0.93
4	1.23	1.23	0.66	1.42	0.87	1.42	1.15
5	1.63	0.58	1.15	0.93	1.15	0.71	1.15
6	1.52	1.63	0.87	0.93	0.87	1	0.81
7	-	1.42	1	0.81	0.87	1.23	1.63
8	-	1.07	0.93	0.81	0.93	0.87	1.52
9	-	1	1.42	0.58	0.71	0.54	0.81
10	-	1.74	0.62	0.54	1.07	0.54	1.23
11	-	1.16	1.42	0.66	0.61	1.15	0.76
12	-	1.23	1.42	0.62	0.87	1.32	0.62
13	-	-	0.71	0.66	0.66	0.76	1.15
14	-	-	0.93	0.71	0.66	0.93	0.62
15	0.87	-	1.15	0.81	0.87	1.23	0.87
16	0.93	0.66	1.15	0.62	0.54	1.07	1.23

In Table 3, at low heat loads applied to the evaporator, the vertical BHM orientation denotes several channels in which the fluid does not present any dominant oscillation within the observation window, thus suggesting that the high intermittency of the overall device operation prevents any identification of the dominant frequencies. At average-high heat loads, a dominant oscillation frequency can be perceived in every channel, confirming the transition from intermittent flow to full activation of the device. In the horizontal orientation (Table 4), a lack of fluid motion hampers a clear identification of a dominant frequency in the overall device at Q = 50 W, while every FPPHP branch denotes fluid oscillations from 100 W up to the maximum provided power input, similarly confirming the transition between the two mentioned working regimes. The listed

fluid oscillation frequencies are in agreement with those typically found with direct fluid visualizations [1,7,15,44,45]. In addition, they confirm the working regimes identified in [29] by means of standard techniques, i.e., evaporator temperature fluctuations, and statistical reduction in wall-to-fluid heat fluxes, for which the overview is reported in Table 5.

Table 4. Dominant oscillation frequencies evaluated in the horizontal orientation for every channel at varying heat load. Dashes stand for absence of dominant fluid oscillation.

f_d [Hz]	Q [W]				
Channel	***50***	***100***	***150***	***200***	***250***
1	-	0.66	0.87	1.07	1.32
2	-	0.66	0.93	1.07	1.15
3	-	0.62	1.87	1.07	1.32
4	-	0.71	0.93	1	1.23
5	-	0.71	0.93	1.07	1.32
6	-	1.42	0.87	1	1.23
7	-	1.42	0.87	1.07	1.23
8	-	1.42	0.93	1	1.23
9	-	0.87	0.81	1.07	1.23
10	-	0.76	0.87	1.07	1.32
11	-	0.66	0.87	1.07	1.23
12	-	0.76	0.87	1	1.23
13	-	0.71	1.74	1.07	1.23
14	-	0.71	0.87	1.07	1.23
15	-	0.66	0.87	1.07	1.32
16	-	0.66	0.93	1.07	1.15

Table 5. Device working regimes identified in [29]. "I": intermittent flow, "F": full activation.

Orientation	***Q* [W]**						
Vertical BHM	*50*	*70*	*90*	*120*	*150*	*200*	*250*
	I	*I*	*F*	*F*	*F*	*F*	*F*
Horizontal	*50*	*100*	*150*	*200*	*250*		
	I	*F*	*F*	*F*	*F*		

5.3. Time Evolution of Fluid Oscillations

The FPPHP oscillatory behavior over time, which was qualitatively observed in scalograms of Section 5.2, was assessed by investigating some of its features, such as continuity and channel activity. Specifically, the continuity t_c is here defined as the persistency of fluid oscillations over time around the dominant frequency, i.e., in the range $B_f = f_d \pm 15\% f_d$. It can be conceptually expressed, for a given device channel, as

$$t_c = \frac{\text{Time during which fluid oscillates at a frequency close to the dominant one}}{\text{Total acquisition time}} \quad (5)$$

Channels activity t_a is instead referred to presence of fluid oscillations:

$$t_a = \frac{\text{Time during which fluid oscillations are perecevibale}}{\text{Total acquisition time}} \quad (6)$$

Both properties are believed to complete the fluid oscillations description in terms of time evolution, providing a better quantification of the device heat transfer capabilities. The evaluation of continuity and activity is based on the time-wise determination of the main oscillation frequencies, i.e., referred to as the power peaks in scalograms. However, a reliable and unambiguous evaluation of scalogram peaks is greatly hampered by the

presence of low-power peaks, which are not always representative of significant fluid oscillations. Hence, a procedure for scalogram denoising, aimed at discerning meaningful from neglectable power peaks, is required. In the present analysis, the *K*-means clustering was employed to highlight high-power regions in scalograms. In particular, such a method relies on an iterative data-partitioning algorithm that assigns *N* observations to *K* separate clusters defined by centroids [46]. *K* is preliminarily chosen, depending on the specific application. The observations assignment relies on within-cluster variance minimizations through the evaluation of squared Euclidean distances from centroids, progressively moved until the minimization condition is satisfied. Given a set of observations $\boldsymbol{O} = \{\boldsymbol{O_1}, \boldsymbol{O_2}, \ldots \boldsymbol{O_n}\}$, the partition into $k \leq K$ subsets $\boldsymbol{S} = \{\boldsymbol{S_1}, \boldsymbol{S_2}, \ldots \boldsymbol{S_k}\}$ is performed according to the following minimization problem:

$$\underset{\boldsymbol{S}}{argmin} \sum_{k=1}^{K} \sum_{s \in \boldsymbol{S_k}} \|s - \mu_k\| \tag{7}$$

where μ_k is the mean of the *k*-th subset. When applied to scalograms, clusters containing residual noise, wavelet artifacts or non-relevant oscillations will present lower *k* coefficients [28]. Areas including significant oscillatory phenomena will instead present high k coefficients. Consequently, the only partitions defined by $k = K$ were considered as meaningful regions, while other partitions were discarded. For the present analysis, the value $K = 4$ was chosen using, as a reference, the one provided by the Calinski–Harabasz criterion [47]. Since the convergence of the *K*-means algorithm is affected by the initial position of centroids, their initialization was replicated until an optimal final partition of scalograms, i.e., a partition capable of identifying with good accuracy the high-power regions, was obtained. In Figure 13a,b, the scalograms of Figure 8 (250 W, Ch12, BHM) and 10 (250 W, Ch12, horizontal) are proposed to clearly present, from a visual standpoint, the steps of the present peak identification procedure. In Figure 13c,d, the corresponding denoised scalograms are shown: the application of the K-means method highlights high-power peaks, while the scalograms low-power background is set to 0. Once the denoising procedure was applied, the scalograms' maximum peaks, i.e., main oscillatory phenomena, could be identified, time instant by time instant. In Figure 13e,f, the time location of frequencies referred to scalogram peaks is shown over time, together with the dominant frequencies (solid lines) and B_f boundaries (dotted lines). As is noticeable, time instants that do not present high-power peaks in the threated scalograms are not assigned to any frequencies (gaps in Figure 13e,f). In addition, time periods exceeding the COIs limits are not considered. When compared to the vertical BHM (Figure 13e), the signal referring to the horizontal orientation (Figure 13f) denotes longer periods of oscillation within Bf, suggesting greater continuity over time. In particular, the continuity time t_t, defined as the total time during which oscillations occur around the dominant frequency, was assessed to be equal to 2.14 s and 8.22 s for the vertical and horizontal orientations, respectively. This confirms the qualitative information provided in Section 5.2. On the other hand, the vertical BHM exhibits an overall longer activity, since oscillations at given frequencies are present for more time within the observation window. The channel activity time was evaluated to be equal to 17.32 s and 12.76 s for the vertical and horizontal orientations, respectively.

The investigation on the continuity of fluid oscillations and channel activity was extended to all FPPHP channels for average and high-power inputs to the evaporator, namely $Q = 150$ W and $Q = 250$ W. Lower heat loads were not considered since either weak or absent fluid oscillations prevented a clear discernment of high-power peaks from low-power backgrounds in scalograms. In Tables 6 and 7, t_c and t_a are listed for the mentioned study cases to present a channel-wise description of continuity and activity. It has to be stressed that the uncertainty, referring to the evaluated times, is strictly linked to the time resolution of the obtained magnitude scalograms. In fact, the time resolution determines the error made in the estimation of the time instants at which maximum powers are identified in scalograms after the denoising procedure. For the given wavelet parameters (Table 2),

the time resolution equals 0.01 s, corresponding to less than 0.1 % of the total observation windows. For both heat loads in the vertical BHM (Table 6), the continuity generally assumes different values from channel to channel with respect to the horizontal orientation (Table 7), confirming that the fluid oscillatory motion is more scattered over a wider range of frequencies. For what concerns activity, the vertical BHM denotes more similar ta values, especially at high heat load, underlining that the fluid oscillations are promoted in every channel by such orientation.

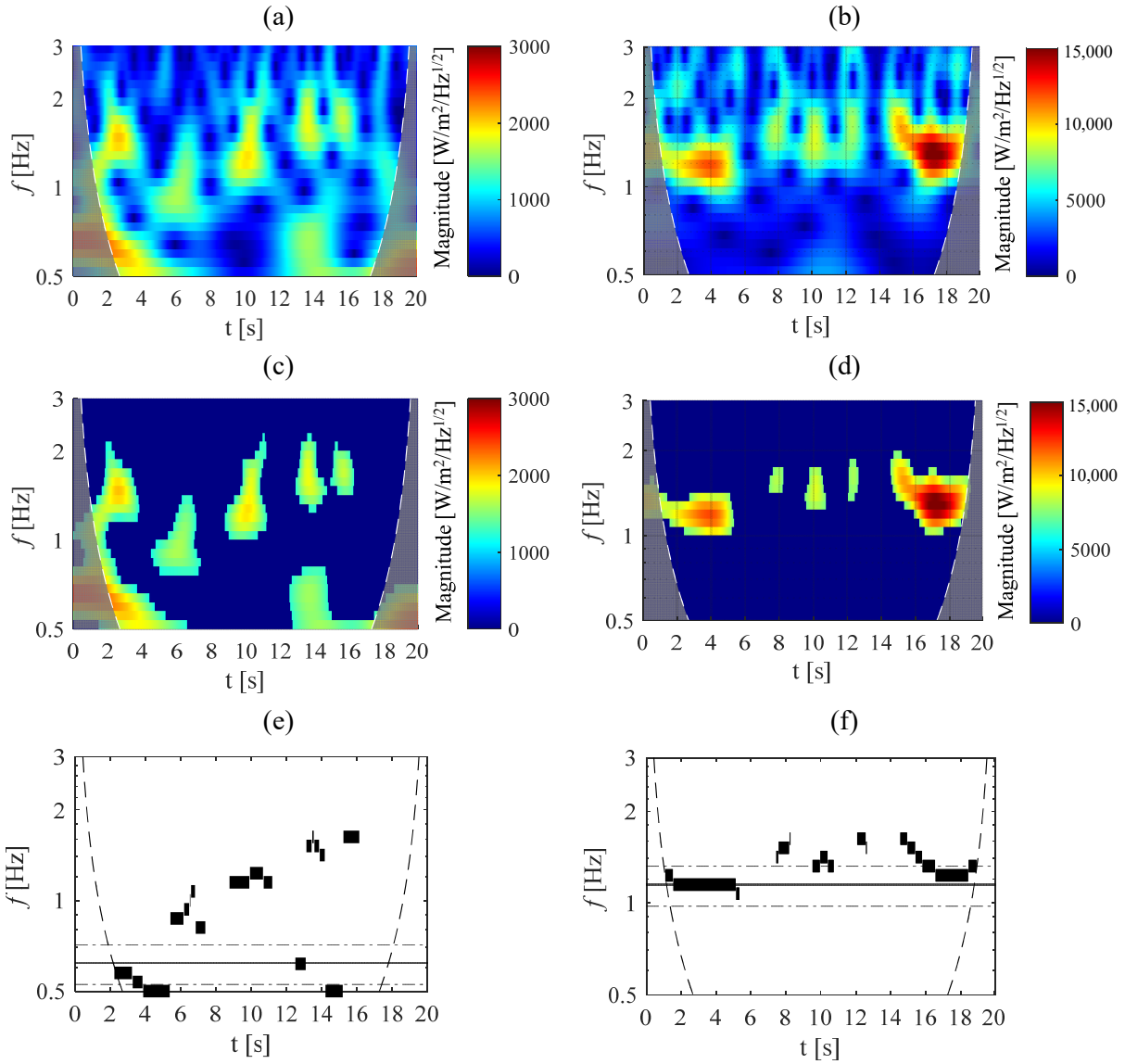


Figure 13. Scalograms referred to channel 12 for the vertical BHM (**a**) and horizontal orientation (**b**), Q = 250 W; denoised scalograms (**c**,**d**) and frequency identification over time (**e**,**f**).

Both continuity and activity values shown in Tables 6 and 7 were therefore averaged over the entire device, i.e., for all channels, resulting in $t_{c,av}$ and $t_{a,av}$, respectively. In Figure 14, $t_{c,av}$ is shown for both considered heat loads and device orientations. The vertical BHM exhibits lower values of $t_{c,av}$ (around 23 and 27% of the total observation window), confirming the greater continuity of oscillations in the horizontal orientation, where $t_{c,av}$ is equal to about 37 and 34% for average and high heat loads, respectively. However, a certain decrease in average continuity time with the increase in heat load is perceivable, denoting a reduction in fluid oscillation around the dominant frequency probably due to the onset of higher inertial forces, i.e., less stable oscillatory behavior [15,16,41]. $t_{a,av}$ is instead shown

in Figure 15 for the same test conditions. Here, the vertical BHM presents generally greater channel activity with respect to the horizontal orientation, since the gravity-assisted mode promotes the fluid motion in the overall device without significant stopovers, confirming what was observed in other works on FPPHPs, where the horizontal orientation usually results in a less stable operation of the device over time [22,39,42]. Additionally, for such an orientation, the activity time increases with the power input, while the horizontal mode presents similar activity times. This remark suggests that above a certain heat load, channel activity saturates in the horizontal orientation probably due to the absence of significant buoyancy forces. Higher activity times of the vertical BHM furthermore confirm the better thermal performance assessed in [29] for such an orientation.

Table 6. Continuity and activity evaluated for the vertical BHM.

Channel	Q [W]			
	150		***250***	
	t_c [%]	t_a [%]	t_c [%]	t_a [%]
1	*17.7*	*52.1*	*28.6*	*89.9*
2	*14*	*88.9*	*30.5*	*91.65*
3	*27.1*	*88.1*	*35.6*	*73.7*
4	*24.2*	*80.1*	*43.4*	*89.9*
5	*5.7*	*47.1*	*31.9*	*79.9*
6	*34.3*	*73.9*	*13.3*	*90.1*
7	*9.6*	*65.1*	*52.9*	*85.7*
8	*11.6*	*87.2*	*25.1*	*93.8*
9	*13.5*	*74.4*	*28.8*	*92.7*
10	*5*	*49.7*	*32.4*	*99.7*
11	*69.5*	*100*	*15.5*	*94.8*
12	*30.2*	*81.8*	*10.7*	*86.6*
13	*36*	*58.4*	*8.7*	*80.5*
14	*46.1*	*80.3*	*21*	*99*
15	*12.5*	*54*	*31.4*	*94.1*
16	*13.2*	*46.8*	*27.8*	*84.7*

Table 7. Continuity and activity evaluated for the horizontal orientation.

Channel	Q [W]			
	150		***250***	
	t_c [%]	t_a [%]	t_c [%]	t_a [%]
1	*46*	*46*	*24.2*	*38.3*
2	*16.9*	*63.1*	*32.4*	*45.8*
3	*15.9*	*56*	*23.2*	*77.5*
4	*18.1*	*83.2*	*26.1*	*72.9*
5	*44.7*	*74.3*	*24.7*	*62.9*
6	*48.8*	*72.8*	*30.1*	*81.6*
7	*34.4*	*65.2*	*36.8*	*85.3*
8	*51.6*	*78.3*	*42.3*	*75.5*
9	*12.6*	*64.8*	*52.5*	*86.2*
10	*52.1*	*81.7*	*23.2*	*75.9*
11	*38.7*	*61*	*27.9*	*73.8*
12	*55.3*	*71.5*	*41.1*	*63.8*
13	*8.7*	*51.3*	*32.6*	*72.2*
14	*47.6*	*71.4*	*30.1*	*86.8*
15	*54.1*	*79.9*	*52.9*	*71.4*
16	*46.6*	*73.4*	*37.6*	*63.8*

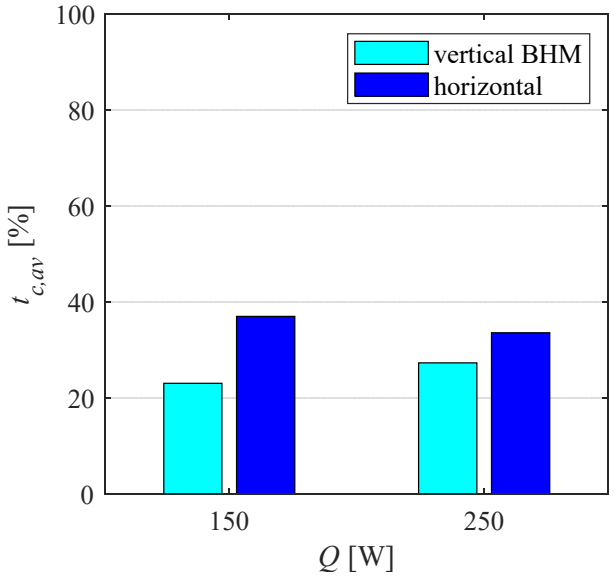


Figure 14. Mean continuity time for average and high heat loads and the two considered orientations.

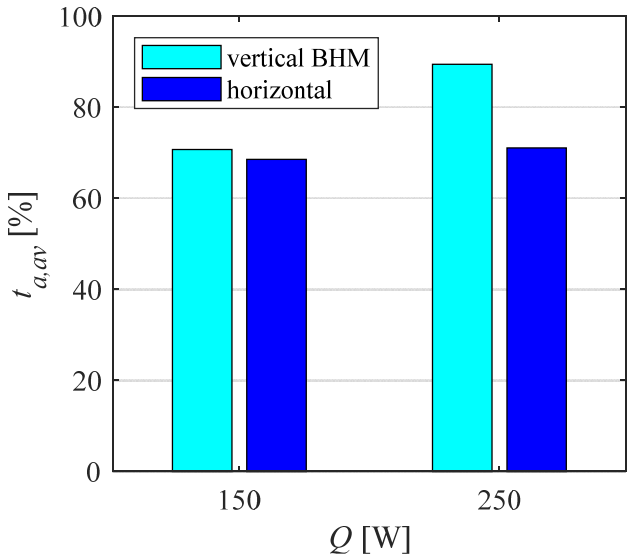


Figure 15. Average activity time of channels as percentage of the observation window length.

5.4. Statistical Description of the Oscillatory Behavior

After providing a quantification of the main properties defining the oscillatory behavior in the studied device, the evaluated channel-wise dominant frequencies were statistically reduced for a complete description of fluid oscillations. To this aim, the arithmetic mean ($f_{d,av}$) and the standard deviation ($f_{d,std}$) of f_d were computed by considering every FPPHP channel. In Figure 16, $f_{d,av}$ and $f_{d,std}$ are shown for the only power inputs to the evaporator in which f_d could be evaluated in every channel of the device, i.e., during its full activation. Here, the average dominant oscillation frequency (Figure 16a) exhibits a general increasing trend, in accordance with other studies also concerning tubular layouts [20,27,48]. For the vertical BHM orientation, $f_{d,av}$ ranges from about 0.78 Hz to 1 Hz, while the horizontal orientation highlights values of $f_{d,av}$ that increase from a minimum of about 0.84 Hz to a maximum of 1.25 Hz, confirming the typical fluid oscillation frequencies found in the literature [2]. It has to be observed that while $f_{d,av}$ denotes a linear increment with the power input to the evaporator in the horizontal orientation, it seems to approach an asymptotic value with the increase in Q in the vertical BHM. This suggests that the semi-annular or annular flow, promoted by the gravity effects on the device at high heat loads, results in

different oscillatory behavior with respect to that in the horizontal orientation (where a slug-plug flow is more likely to occur), probably due to significantly different phase-change phenomena. In fact, at high heat loads, significant fluid motion towards the condenser may occur, while liquid backflow by gravity may be, to some extent, less predominant during operation, affecting the overall oscillatory behavior, which is in agreement with [27]. Additionally, the standard deviation of f_d (Figure 16b) highlights a different behavior in terms of oscillations from channel to channel in the vertical BHM orientation, which persists even during the full activation of the device. For the horizontal orientation, $f_{d,std}$ seems to decrease instead with the increasing of the power input, suggesting that during the full activation, every channel approaches the same oscillatory behavior. This is probably due to the fact that when buoyancy forces are negligible, as in the horizontal orientation, flow reactivations may occur in a waveform over the entire device, leading to similar fluid oscillation frequencies [19,42,49].

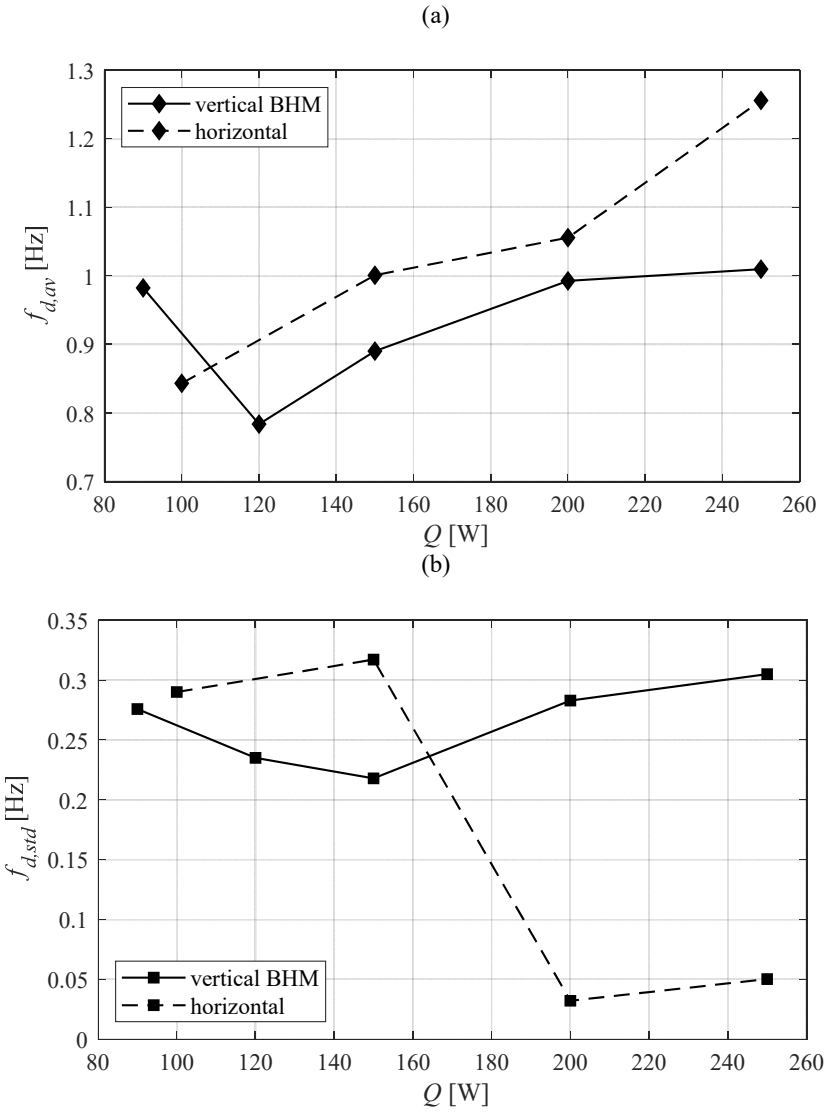


Figure 16. Average dominant fluid oscillation frequency in the overall device (**a**) and channel-wise standard deviation (**b**) for the two considered FPPHP orientations.

5.5. Link between Fluid Oscillations and Transverse Interactions

During its operation, the thermal performance of a FPPHP might be significantly influenced by thermal interactions occurring between adjacent channels, which lead to a homogenization of temperature and, consequently, of the driven force for the working fluid

motion in the overall two-phase device [16,50]. A local heat transfer analysis could thus be required to attempt a description of conduction between adjacent channels in FPPHPs. To this aim, the temperature distributions acquired by means of thermography, and properly regularized as thoroughly explained in [29], were adopted to provide an estimation of the heat flux exchanged between the n-th and $(n + 1)$-th channels by conduction $q_{Fou,n\to n+1}$, according to Fourier's law (along y-axis as defined in Figure 3):

$$q_{Fou,n\to n+1}(z,t) = -k\frac{\partial T(y,z,t)}{\partial y} \tag{8}$$

In particular, the partial derivative of T is evaluated in the median point between adjacent channels for every axial coordinate z as a function of time. The values averagely assumed by q_{Fou} over time were therefore adopted to estimate the power transferred by transverse conduction $Q_{tr_{cond}}$ between every adjacent channel pair in the overall device along the adiabatic section (green box in Figure 1b) as follows:

$$Q_{tr_{cond}} = \frac{\sum_{n=1}^{num-1}\left\{\left|\sum_{z=0}^{L_{adiab}} mean[q_{Fou,n\to n+1}(z,t=1\ldots N)\right]\cdot\Delta z\cdot T_{FPPHP}|\right\}}{num-1} \tag{9}$$

where num is the total number of FPPHP channels, mean is the arithmetic mean operator, N is the total number of time samples, L_{adiab} is the length of the adiabatic section framed by the IR camera, Δz is the distance between two consecutive pixels in the z direction of the thermographic data, and T_FPPHP is the device thickness. Finally, $Q_{tr_{cond}}$ was normalized with respect to the net power input to the evaporator divided by the number of FPPHP channels, resulting in $Q_{ratio} = Q_{tr_{cond}}/(\frac{Q}{num})$. Specifically, Q_{ratio} defines the percentage of transverse conduction with respect to the power potentially transferrable by a single FPPHP branch from the evaporator to the condenser. In Figure 17, Q_{ratio} is shown as a function of Q for both considered device orientations. For the vertical BHM, the effects of transverse conduction become more and more negligible as the power input to the evaporator increases. For the horizontal orientation, Q_{ratio} is almost equal to 15% at high power inputs, denoting instead strong conductive effects between adjacent channels in agreement with other literature findings [29,30,39,51]. In fact, operating a FPPHP in horizontal orientation generally leads to a higher evaporator temperature due to lower thermal performances, eventually increasing the temperature of the fluid flowing towards the condenser. This may result in greater temperature gradients between adjacent branches, leading to higher thermal interactions between the working fluid and the side walls of the channels and, consequently, to stronger transverse interactions.

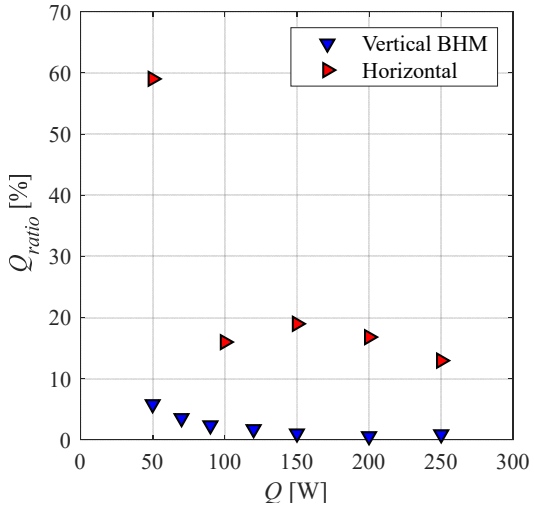


Figure 17. Q_{ratio} as a function of the power input to the evaporator for both considered device orientations.

The highlighted variation in terms of transverse conduction from vertical BHM to horizontal orientation may be due to different oscillatory and local heat transfer behaviors of the FPPHP, which are strictly linked to wall-to-fluid heat transfer interactions. To investigate the interplay between the local wall-to-fluid heat flux and transverse conduction $q_{Fou,7\to8}$, the heat flux q exchanged in two branches, i.e., channels 7 and 8, was compared with the corresponding heat flux $q_{Fou,7\to8}$ (z = 0.02 m) in terms of oscillation frequency. In Figure 18a, all the mentioned heat fluxes related to the vertical BHM are shown for Q = 200 W. In Figure 18b, the power spectra resulting from the wavelet method of Section 3.2 are instead provided, highlighting no dominant frequency indicative of the $q_{Fou,7\to8}$ signal. The scalograms that referred to the analyzed signals were not considered, since only the power spectra were believed to be more accurate in underlying differences or similarities between the compared, overall oscillatory behaviors. A similar comparison was carried out in Figure 19 for the horizontal orientation, where all considered signals exhibited the same dominant frequency. In fact, in such an orientation, the fluid similarly oscillates in both FPPHP branches and the regular slug-plug motion results in stronger transverse conduction between adjacent channels. This negative effect is furthermore enhanced by greater amplitudes of q during the horizontal operation, which lead to higher wall temperature variations within the adiabatic section. On the contrary, in the vertical BHM, the greater chaoticity of the fluid motion and different flow pattern, coupled with low-amplitude values of q, seem to prevent the channels from thermally interacting with each other, leading to weaker transverse conduction.

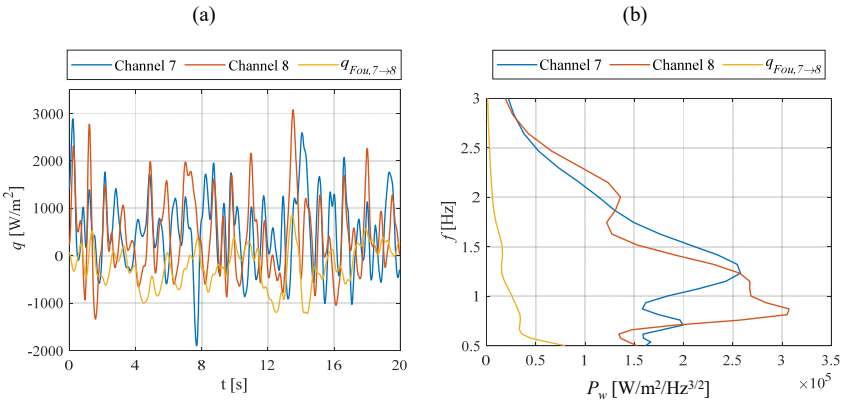


Figure 18. Wall-to-fluid heat fluxes corresponding to channel 7 and 8, heat flux by transverse conduction $q_{Fou,7\to8}$ (**a**), and corresponding power spectra (**b**) for the vertical BHM at Q = 200 W and z = 0.02 m.

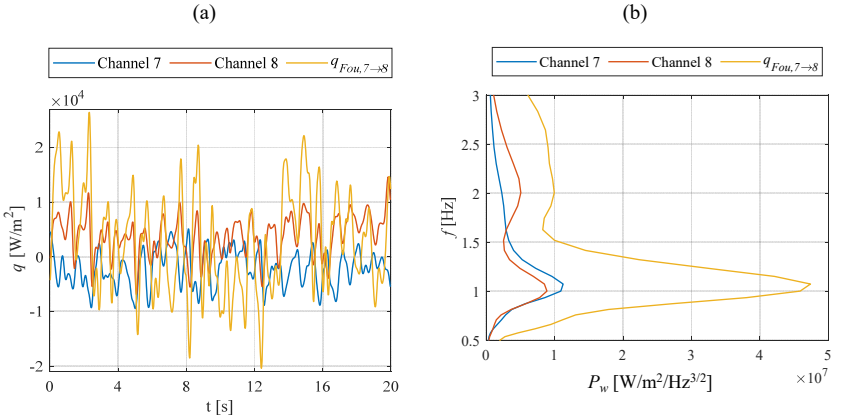


Figure 19. Wall-to-fluid heat fluxes corresponding to channel 7 and 8, heat flux by transverse conduction $q_{Fou,7\to8}$ (**a**), and corresponding power spectra (**b**) for the horizontal orientation at Q = 200 W and z = 0.02 m.

6. Conclusions

The presented study concluded the analysis on the global and local thermal behavior of a fully metallic flat-plate pulsating heat pipe, first discussed in [29]. The aim of the present work was to design a novel approach for the study of the inner fluid dynamics in FPPHPs without taking advantage of any direct fluid visualizations, which represent most of the experimental studies on flow behavior in such heat transfer systems. The wall-to-fluid heat fluxes, evaluated within the adiabatic section of the device by means of thermographic acquisitions on its outer surface, were processed by the wavelet method to estimate dominant fluid oscillation frequencies at varying heat loads and orientations. A validation procedure on synthetic data was carried out to assess the reliability of the estimation procedure. Scalograms (i.e., time-frequency representation of the wavelet transform) were introduced to give useful references for the interpretation of fluid motion in terms of time evolution of the oscillatory phenomena. The characteristic frequencies of the system were furthermore assessed in every device branch by means of power spectra of the considered signals, thus providing a channel-wise description of the fluid motion. The K-means clustering method was used for peak identification in scalograms; two quantitative parameters, namely the average continuity time of oscillations $t_{t,av}$ and the average activity time of channels, were consequently proposed for the description of the device oscillatory behavior over time. The average $f_{d,av}$ and standard deviation $f_{d,std}$ of channel-wise dominant frequencies were therefore evaluated for the whole device to give an overview on the global oscillatory modes. Finally, thermal interactions between adjacent channels were estimated through the Q_{ratio} parameter and explained in terms of fluid oscillation frequencies. The following remarks can be drawn from the present study:

- The higher average activity of channels found in the vertical bottom heated mode confirms its better heat transfer capability with respect to the horizontal orientation, even though values of $t_{c,av}$ equal to 23 and 27% of the total observation window at average and high heat loads, respectively, highlight a lower continuity of fluid oscillations in the vertical operation;
- The generally greater continuity of oscillations in the horizontal orientation is also established by the $f_{d,std}$ values, which suggest more similar dominant fluid oscillation frequencies among the device branches especially at high heat loads, where $f_{d,std}$ is set below 0.05 Hz;
- For the vertical BHM orientation, $f_{d,av}$ ranges from 0.78 Hz up to 1 Hz during the device's full activation, while the horizontal orientation exhibits values of $f_{d,av}$ that increase from a minimum of about 0.84 Hz to a maximum of 1.25 Hz;
- The heat transferred by conduction between adjacent channels is higher in the horizontal orientation, where Q_{ratio} ranges from about 60% at low heat loads to 15% at high heat loads;
- Similar oscillatory behaviors in adjacent channels increase the magnitude of transverse thermal interactions.

In conclusion, the presented results quantified the oscillatory behavior of the investigated device. The working regimes assessed in [29] of the analysis were confirmed by the data, thus giving a deeper insight into the heat transfer modes of the device without adopting any transparent sections for direct fluid visualizations. In view of the results, the adopted technique provided a good insight into the inner fluid dynamics and the overall thermal behavior of the studied device, in accordance with what was observed in previous experimental works relying on different experimental approaches. The here-proposed method for fluid flow assessment can thus be extended to other flat-plate layouts, having walls made entirely of metallic material to give interesting pieces of data for both the augmentation of the literature dataset in terms of fluid oscillation frequencies, and the improvement of existing numerical and theoretical models. To provide a comprehensive summarization of all the results collected in both parts of the experimental work ([29] and present investigation), the main evaluated quantities are listed in Tables 8 and 9 for the vertical bottom heated mode and the horizontal orientation, respectively. Here, R_{eq} is the

evaluated equivalent thermal resistance of the device, *cvt* and *cvs* are the coefficients of variation of the wall-to-fluid heat flux over time and along space, respectively, and q_{80} is the 80th percentile of the heat flux.

Table 8. Evaluated quantities for the vertical bottom heated mode orientation. Green and red colors refer to the intermittent flow and the full activation regime, respectively.

		Q [W]						
	Units	***50***	***70***	***90***	***120***	***150***	***200***	***250***
R_{eq}	[K/W]	0.3	0.2	0.12	0.11	0.09	0.08	0.07
cvt_{av}	[%]	49.0	60.5	74.7	72.0	72.2	72	70.07
cvt_{std}	[%]	17.0	14.6	11.3	13.7	13.3	5.6	7.5
cvs_{av}	[%]	57.0	47.7	44.7	44.9	43.6	43.2	44.6
cvs_{std}	[%]	19.5	17.8	10.7	13.2	10.6	9.9	8.6
q_{80}	[W/m^2]	1068	1117	945.9	1306	1364	1435	2314
$f_{d,av}$	[Hz]	-	-	0.98	0.78	0.89	0.99	1.01
$f_{d,std}$	[Hz]	-	-	0.28	0.24	0.22	0.28	0.3

Table 9. Evaluated quantities for the horizontal orientation. Green and red colors refer to the intermittent flow and the full activation regime, respectively.

		Q [W]				
	Units	***50***	***100***	***150***	***200***	***250***
R_{eq}	[K/W]	0.48	0.19	0.14	0.11	0.09
cvt_{av}	[%]	70.7	74.4	69.7	68.4	68.0
cvt_{std}	[%]	25.9	11.0	6.4	5.2	4.0
cvs_{av}	[%]	70.03	53.2	48.5	48.4	50.4
cvs_{std}	[%]	18.23	10.5	9.1	7.0	5.8
q_{80}	[W/m^2]	1086	1995	3594	5321	7149
$f_{d,av}$	[Hz]	-	0.84	1	1.06	1.26
$f_{d,std}$	[Hz]	-	0.29	0.31	0.03	0.05

Author Contributions: Conceptualization, L.P., L.C. and F.B.; Methodology, L.P., L.C. and F.B.; Software, L.P.; Validation, L.P., M.S. and C.R.; Formal analysis, L.P. and C.R.; Investigation, M.S. and C.R.; Resources, F.B.; Data curation, L.P. and L.C.; Writing—original draft, L.P.; Writing—review & editing, L.C., V.A., M.S. and F.B.; Visualization, M.S.; Supervision, L.C., V.A. and F.B.; Project administration, V.A. and F.B.; Funding acquisition, V.A. and F.B. All authors have read and agreed to the published version of the manuscript.

Funding: This research was funded by the European Space Agency (ESA) grant number 4000128640/19/NL/PG/pt, ESA MAP project TOPDESS.

Institutional Review Board Statement: Not applicable.

Informed Consent Statement: Not applicable.

Data Availability Statement: The data presented in this study are available on request from the corresponding authors. The data are not publicly available due to the large dataset.

Acknowledgments: The work has been carried out through a fruitful and effective collaboration between the University of Parma and PPRIME Institute—ENSMA (Poitiers). The authors would like to acknowledge the European Space Agency (ESA)'s support.

Conflicts of Interest: The authors declare no conflict of interest. The funders had no role in the design of the study; in the collection, analyses, or interpretation of data; in the writing of the manuscript; or in the decision to publish the results.

Nomenclature

Symbol	Quantity	SI Unit
W_ψ	Wavelet transform	-
ω_0	Wavelet angular frequency	rad/s
σ	Standard deviation	K
a	Wavelet scale	Hz^{-1}
Amp	Amplitude of analytical heat flux	W/m^2K
f	Frequency	Hz
f_{max}	Wavelet maximum frequency	Hz
f_{min}	Wavelet minimum frequency	Hz
g	General time-dependent signal	-
i	Imaginary part	-
k	Coefficient of conduction	W/mK
L_{adiab}	Length of the adiabatic section (within the observation window)	m
n	Channel number	-
N	Total number of time samples of the heat flux distributions	-
num	Total number of channels	-
P_w	Power spectrum magnitude	-
q	Wall-to-fluid heat flux per unit surface	W/m^2K
Q	Heat load to the evaporator	W
q_{exact}	Synthetic heat flux	W/m^2K
q_{Fou}	Heat exchanged between adjacent channels	W/m^2K
Q_{ratio}	Power transferred by transverse conduction by a single channel, divided by power transferrable from evaporator to condenser	%
$q_{restored}$	Restored synthetic heat flux	W/m^2K
Q_{TRcond}	Transverse conduction between channels pairs	W/m^2K
t	Time	s
t_a	Activity time	%
t_c	Continuity time	%
T_{FPPHP}	Device thickness	m
z	Axial coordinate	m
η	Dimensionless time	-
τ	Wavelet time shift	s
ψ	Wavelet	-
Subscripts, superscripts		
av	Average	
d	Dominant	
std	Standard deviation	

References

1. Spinato, G.; Borhani, N.; Thome, J.R. Understanding the self-sustained oscillating two-phase flow motion in a closed loop pulsating heat pipe. *Energy* **2015**, *90*, 889–899. [CrossRef]
2. Marengo, M.; Nikolayev, V.S. Pulsating Heat Pipes: Experimental Analysis. *Des. Appl.* **2018**, 1–62. [CrossRef]
3. Murshed, S.M.S.; de Castro, C.A.N. A critical review of traditional and emerging techniques and fluids for electronics cooling. *Renew. Sustain. Energy Rev.* **2017**, *78*, 821–833. [CrossRef]
4. Nazari, M.A.; Ahmadi, M.H.; Ghasempour, R.; Shafii, M.B.; Mahian, O.; Kalogirou, S.; Wongwises, S. A review on pulsating heat pipes: From solar to cryogenic applications. *Appl. Energy* **2018**, *222*, 475–484. [CrossRef]
5. Ishii, K.; Fumoto, K. Temperature visualization and investigation inside evaporator of pulsating heat pipe using temperature-sensitive paint. *Appl. Therm. Eng.* **2019**, *155*, 575–583. [CrossRef]
6. Perna, R.; Abela, M.; Mameli, M.; Mariotti, A.; Pietrasanta, L.; Marengo, M.; Filippeschi, S. Flow characterization of a pulsating heat pipe through the wavelet analysis of pressure signals. *Appl. Therm. Eng.* **2020**, *171*, 115128. [CrossRef]
7. Xu, J.L.; Zhang, X.M. Start-up and steady thermal oscillation of a pulsating heat pipe. *Heat Mass Transf.* **2005**, *41*, 685–694. [CrossRef]
8. Karthikeyan, V.K.; Ramachandran, K.; Pillai, B.C.; Solomon, A.B. Understanding thermo-fluidic characteristics of a glass tube closed loop pulsating heat pipe: Flow patterns and fluid oscillations. *Heat Mass Transf.* **2015**, *51*, 1669–1680. [CrossRef]

9. Takawale, A.; Abraham, S.; Sielaff, A.; Mahapatra, P.S.; Pattamatta, A.; Stephan, P. A comparative study of flow regimes and thermal performance between flat plate pulsating heat pipe and capillary tube pulsating heat pipe. *Appl. Therm. Eng.* **2019**, *149*, 613–624. [CrossRef]
10. Mameli, M.; Marengo, M.; Khandekar, S. Local heat transfer measurement and thermo-fluid characterization of a pulsating heat pipe. *Int. J. Therm. Sci.* **2014**, *75*, 140–152. [CrossRef]
11. Monroe, J.G.; Aspin, Z.S.; Fairley, J.D.; Thompson, S.M. Analysis and comparison of internal and external temperature measurements of a tubular oscillating heat pipe. *Exp. Therm. Fluid Sci.* **2017**, *84*, 165–178. [CrossRef]
12. Fairley, J.D.; Thompson, S.M.; Anderson, D. Time–frequency analysis of flat-plate oscillating heat pipes. *Int. J. Therm. Sci.* **2015**, *91*, 113–124. [CrossRef]
13. Pagliarini, L.; Cattani, L.; Bozzoli, F.; Mameli, M.; Filippeschi, S.; Rainieri, S.; Marengo, M. Thermal characterization of a multi-turn pulsating heat pipe in microgravity conditions: Statistical approach to the local wall-to-fluid heat flux. *Int. J. Heat Mass Transf.* **2021**, *169*, 120930. [CrossRef]
14. Iwata, N.; Bozzoli, F.; Pagliarini, L.; Cattani, L.; Vocale, P.; Malavasi, M.; Rainieri, S. Characterization of thermal behavior of a micro pulsating heat pipe by local heat transfer investigation. *Int. J. Heat Mass Transf.* **2022**, *196*, 123203. [CrossRef]
15. Ayel, V.; Slobodeniuk, M.; Bertossi, R.; Romestant, C.; Bertin, Y. Flat plate pulsating heat pipes: A review on the thermohydraulic principles, thermal performances and open issues. *Appl. Therm. Eng.* **2021**, *197*, 117200. [CrossRef]
16. Khandekar, S. Thermofluid dynamic study of flat-plate closed-loop pulsating heat pipes. *Microscale Thermophys. Eng.* **2003**, *6*, 303–317. [CrossRef]
17. Slobodeniuk, M.; Bertossi, R.; Ayel, V.; Ravichandran, R.; Thyagarajan, K.; Romestant, C.; Bertin, Y. Experimental study of the flat plate pulsating heat pipe operation during dry-out and flow re-activation periods under microgravity conditions. *Int. J. Multiph. Flow* **2022**, *147*, 103888. [CrossRef]
18. Pietrasanta, L.; Mameli, M.; Mangini, D.; Georgoulas, A.; Michè, N.; Filippeschi, S.; Marengo, M. Developing flow pattern maps for accelerated two-phase capillary flows. *Exp. Therm. Fluid Sci.* **2020**, *112*, 109981. [CrossRef]
19. Miyazaki, Y. Oscillatory flow in oscillating heat pipe. In Proceedings of the 11th International Heat Pipe Conference, Tokyo, Japan, 12–16 September 1999; pp. 367–372.
20. Borgmeyer, B.; Ma, H.B. Experimental Investigation of Oscillating Motions in a Flat Plate Pulsating Heat Pipe. *J. Thermophys. Heat Transf.* **2007**, *21*, 405–409. [CrossRef]
21. Pagnoni, F.; Ayel, V.; Scoletta, E.; Bertin, Y. Experimental and numerical analysis of a closed-loop flat-plate pulsating heat pipe: Effects of orientation with respect to gravity on the thermohydraulic behavior. In Proceedings of the International Heat Transfer Conference Digital Library, Beijing, China, 10–15 August 2018.
22. Jun, S.; Kim, S.J. Experimental study on a criterion for normal operation of pulsating heat pipes in a horizontal orientation. *Int. J. Heat Mass Transf.* **2019**, *137*, 1064–1075. [CrossRef]
23. Yoon, A.; Kim, S.J. Experimental and theoretical studies on oscillation frequencies of liquid slugs in micro pulsating heat pipes. *Energy Convers. Manag.* **2019**, *181*, 48–58. [CrossRef]
24. Dreiling, R.; Zimmermann, S.; Nguyen-Xuan, T.; Schreivogel, P.; di Mare, F. Thermal resistance modeling of flat plate pulsating heat pipes. *Int. J. Heat Mass Transf.* **2022**, *189*, 122668. [CrossRef]
25. Odagiri, K.; Wolk, K.; Cappucci, S.; Morellina, S.; Roberts, S.; Pate, A.; Furst, B.; Sunada, E.; Daimaru, T. Three-dimensional heat transfer analysis of flat-plate oscillating heat pipes. *Appl. Therm. Eng.* **2021**, *195*, 117189. [CrossRef]
26. Thompson, S.M.; Ma, H.B.; Wilson, C. Investigation of a flat-plate oscillating heat pipe with Tesla-type check valves. *Exp. Therm. Fluid Sci.* **2011**, *35*, 1265–1273. [CrossRef]
27. Yasuda, Y.; Nabeshima, F.; Horiuchi, K.; Nagai, H. Visualization of the working fluid in a flat-plate pulsating heat pipe by neutron radiography. *Int. J. Heat Mass Transf.* **2022**, *185*, 122336. [CrossRef]
28. Zhang, F.Z.; Winholtz, R.A.; Black, W.J.; Wilson, M.R.; Taub, H.; Ma, H.B. Effect of Hydrophilic Nanostructured Cupric Oxide Surfaces on the Heat Transport Capability of a Flat-Plate Oscillating Heat Pipe. *J. Heat Transf.* **2016**, *138*, 062901. [CrossRef]
29. Pagliarini, L.; Cattani, L.; Slobodeniuk, M.; Ayel, V.; Romestant, C.; Bozzoli, F.; Rainieri, S. Novel Infrared Approach for the Evaluation of Thermofluidic Interactions in a Metallic Flat-Plate Pulsating Heat Pipe. *Appl. Sci.* **2022**, *12*, 11682. [CrossRef]
30. Ayel, V.; Slobodeniuk, M.; Bertossi, R.; Karmakar, A.; Martineau, F.; Romestant, C.; Bertin, Y.; Khandekar, S. Thermal performances of a flat-plate pulsating heat pipe tested with water, aqueous mixtures and surfactants. *Int. J. Therm. Sci.* **2022**, *178*, 107599. [CrossRef]
31. Morozov, V.A. *Methods for Solving Incorrectly Posed Problems*; Springer: Berlin/Heidelberg, Germany, 1984.
32. Cattani, L.; Mangini, D.; Bozzoli, F.; Pietrasanta, L.; Miche', N.; Mameli, M.; Filippeschi, S.; Rainieri, S.; Marengo, M. An original look into pulsating heat pipes: Inverse heat conduction approach for assessing the thermal behaviour. *Therm. Sci. Eng. Prog.* **2019**, *10*, 317–326. [CrossRef]
33. Lilly, J.M. Element analysis: A wavelet-based method for analysing time-localized events in noisy time series. *Proc. R. Soc. A Math. Phys. Eng. Sci.* **2017**, *473*, 20160776.
34. Nobach, H.; Tropea, C.; Cordier, L.; Bonnet, J.P.; Delville, J.; Lewalle, J.; Farge, M.; Schneider, K.; Adrian, R. Review of some fundamentals of data processing. In *Springer Handbooks*; Springer: Berlin/Heidelberg, Germany, 2007; pp. 1337–1398.
35. Cui, X.; Zhu, Y.; Li, Z.; Shun, S. Combination study of operation characteristics and heat transfer mechanism for pulsating heat pipe. *Appl. Therm. Eng.* **2014**, *65*, 394–402. [CrossRef]

36. Karthikeyan, V.K.; Khandekar, S.; Pillai, B.C.; Sharma, P.K. Infrared thermography of a pulsating heat pipe: Flow regimes and multiple steady states. *Appl. Therm. Eng.* **2014**, *62*, 470–480. [CrossRef]
37. Mameli, M.; Manno, V.; Filippeschi, S.; Marengo, M. Thermal instability of a Closed Loop Pulsating Heat Pipe: Combined effect of orientation and filling ratio. *Exp. Therm. Fluid Sci.* **2014**, *59*, 222–229. [CrossRef]
38. Betancur-Arboleda, L.A.; Mera, J.P.F.; Mantelli, M. Experimental study of channel roughness effect in diffusion bonded pulsating heat pipes. *Appl. Therm. Eng.* **2020**, *166*, 114734. [CrossRef]
39. Jun, S.; Kim, S.J. Comparison of the thermal performances and flow characteristics between closed-loop and closed-end micro pulsating heat pipes. *Int. J. Heat Mass Transf.* **2016**, *95*, 890–901. [CrossRef]
40. Kearney, D.J.; Suleman, O.; Griffin, J.; Mavrakis, G. Thermal performance of a PCB embedded pulsating heat pipe for power electronics applications. *Appl. Eng.* **2016**, *98*, 798–809. [CrossRef]
41. Qu, J.; Wu, H. Flow visualization of silicon-based micro pulsating heat pipes. *Sci. China Technol. Sci.* **2010**, *53*, 984–990. [CrossRef]
42. Ayel, V.; Araneo, L.; Marzorati, P.; Romestant, C.; Bertin, Y.; Marengo, M. Visualization of Flow Patterns in Closed Loop Flat Plate Pulsating Heat Pipe Acting as Hybrid Thermosyphons under Various Gravity Levels. *Heat Transf. Eng.* **2019**, *40*, 227–237. [CrossRef]
43. Mameli, M.; Araneo, L.; Filippeschi, S.; Marelli, L.; Testa, R.; Marengo, M. Thermal response of a closed loop pulsating heat pipe under a varying gravity force. *Int. J. Therm. Sci.* **2014**, *80*, 11–22. [CrossRef]
44. Kim, J.-S.; Bui, N.H.; Jung, H.-S.; Lee, W.-H. The study on pressure oscillation and heat transfer characteristics of oscillating capillary tube heat pipe. *KSME Int. J.* **2003**, *17*, 1533–1542. [CrossRef]
45. Khandekar, S.; Gautam, A.P.; Sharma, P.K. Multiple quasi-steady states in a closed loop pulsating heat pipe. *Int. J. Therm. Sci.* **2009**, *48*, 535–546. [CrossRef]
46. Frank, I.E.; Todeschini, R. *The Data Analysis Handbook*; Elsevier: Amsterdam, The Netherlands, 1994.
47. Caliński, T.; Harabasz, J. A dendrite method for cluster analysis. *Commun. Stat.* **1974**, *3*, 1–27. [CrossRef]
48. Zhang, Y.; Faghri, A. Advances and unsolved issues in pulsating heat pipes. *Heat Transf. Eng.* **2008**, *29*, 20–44. [CrossRef]
49. Kim, J.-S.; Bui, N.H.; Kim, J.-W.; Kim, J.-H.; Jung, H.S. Flow visualization of oscillation characteristics of liquid and vapor flow in the oscillating capillary tube heat pipe. *KSME Int. J.* **2003**, *17*, 1507–1519. [CrossRef]
50. Noh, H.Y.; Yoon, A.; Kim, S.J. Investigation into the effect of transverse condudction on the thermal performance of a flat-plate pulsating heat pipe. *Int. J. Heat Mass Transf.* **2021**, *181*, 121842. [CrossRef]
51. Yang, H.; Khandekar, S.; Groll, M. Performance characteristics of pulsating heat pipes as integral thermal spreaders. *Int. J. Therm. Sci.* **2009**, *48*, 815–824. [CrossRef]

Disclaimer/Publisher's Note: The statements, opinions and data contained in all publications are solely those of the individual author(s) and contributor(s) and not of MDPI and/or the editor(s). MDPI and/or the editor(s) disclaim responsibility for any injury to people or property resulting from any ideas, methods, instructions or products referred to in the content.